Title

- Full title: Coupling chromatin structure and dynamics by live super-resolution imaging
- Short title: Coupling chromatin structure and dynamics

Authors

R. Barth[1, 2,] K. Bystricky[1] and H. A. Shaban[,1, 3, †, *]

Affiliations

1: Laboratoire de Biologie Moléculaire Eucaryote (LBME), Centre de Biologie Intégrative (CBI), CNRS; University of Toulouse, UPS; 31062 Toulouse; France. 2: Department of Bionanoscience, Delft University of Technology, 2628 CJ Delft, The Netherlands. 3: Spectroscopy Department, Physics Division, National Research Centre, Dokki, 12622 Cairo, Egypt.

†: Present address: Center for Advanced Imaging, Northwest Building, Harvard University, Cambridge, MA, 02138, USA.

*: To whom correspondence may be addressed: Haitham A. Shaban. Email hshaban@fas.harvard.edu

Abstract

Chromatin conformation regulates gene expression and thus constant remodeling of chromatin structure is essential to guarantee proper cell function. To gain insight into the spatio-temporal organization of the genome, we employ high-density photo-activated localization microscopy and deep learning to obtain temporally resolved super-resolution images of chromatin *in vivo*. In combination with high-resolution dense motion reconstruction, we confirm the existence of elongated ~ 45 to 90 nm wide chromatin 'blobs', which appear to be dynamically associating chromatin fragments in close physical and genomic proximity and adopt TAD-like interactions in the time-average limit. We found the chromatin structure exhibits a spatio-temporal correlation extending ~ 4 µm in space and tens of seconds in time, while chromatin dynamics are correlated over ~ 6 µm and outlast 40 s. Notably, chromatin structure and dynamics are closely interrelated, which may constitute a mechanism to grant access to regions with high local chromatin concentration.

Introduction

The three-dimensional organization of the eukaryotic genome plays a central role in gene regulation (*1–3*). Its spatial organization has been prominently characterized by molecular and cellular approaches including high-throughput chromosome conformation capture (Hi-C) (*4*) and fluorescent in situ hybridization (FISH) (*5*). Topologically associated domains (TADs), genomic regions that display a high degree of interaction, were revealed and found to be a key architectural feature (*6*). Direct 3D localization microscopy of the chromatin fiber at the nanoscale (*7*) confirmed the presence of TADs in single cells but also, among others, revealed great structural variation of chromatin architecture (*8*, *9*). To comprehensively resolve the spatial heterogeneity of chromatin, super-resolution microscopy must be employed. Previous work showed that nucleosomes are distributed as segregated, nanometer-sized accumulations throughout the nucleus (*10–13*) and that the epigenetic state of a locus has a large impact on its folding (*14*, *15*). However, to resolve the fine structure of chromatin, high labeling densities, long acquisition times and, often, cell fixation are required. This precludes capturing dynamic processes of chromatin in single live cells, yet chromatin moves at different spatial and temporal scales.

The first efforts to relate chromatin organization and its dynamics were made using a combination of Photo-activated Localization Microscopy (PALM) and tracking of single nucleosomes (*16*). It could be shown that nucleosomes mostly move coherently with their underlying domains, in accordance with conventional microscopy data (*17*); however, a quantitative link between the observed dynamics and the surrounding chromatin structure could not yet be established in real-time. Although it is becoming increasingly clear that chromatin motion and long-range interactions are key to genome organization and gene regulation (*18*), tools to detect and to define bulk chromatin motion simultaneously at divergent spatio-temporal scales and high resolution are still missing.

Here we apply deep learning-based photo-activated localization microscopy (Deep-PALM) for temporally resolved super-resolution imaging of chromatin *in vivo*. Deep-PALM acquires a single resolved image in a few hundred milliseconds with a spatial resolution of ~ 60 nm. We observed elongated ~ 45 to 90 nm wide chromatin domain 'blobs'. Employing a computational chromosome model, we inferred that blobs are highly dynamic entities, which dynamically assemble and disassemble. Consisting of chromatin in close physical and genomic proximity, blobs nevertheless adopt TAD-like interaction patterns when chromatin confirmations are averaged over time. Using a combination of Deep-PALM and high-resolution dense motion reconstruction (*19*), we simultaneously analyzed both structural and dynamic properties of chromatin. Our analysis emphasizes the presence of spatio-temporal cross-correlations between chromatin structure and dynamics, extending several micrometers in space and tens of seconds in time. Furthermore, extraction and statistical mapping of multiple observables from the dynamic behavior of chromatin blobs shows that local chromatin density regulates local chromatin dynamics.

Results

Deep-PALM reveals dynamical chromatin remodeling in living cells.

Super-resolution imaging of complex and compact macromolecules such as chromatin requires dense labeling of the chromatin fiber in order to resolve fine features. We employ Deep-STORM, a method which uses a deep convolutional neural network (CNN) to predict super-resolution images from stochastically blinking emitters (*20*) (Figure 1A; Materials and Methods). The CNN was trained to specific labeling densities for live-cell chromatin imaging using a photo-activated fluorophore (PATagRFP); we therefore refer to the method as Deep-PALM. We chose three labeling densities 4, 6 and 9 emitters per μm^2 per frame in the ON-state to test, based on the comparison of simulated and experimental wide field images (Supplementary Figure 1A). The CNN trained with 9 emitters per μm^2 performed significantly worse than the other CNNs and was

thus excluded from further analysis (Supplementary Figure 1B; Materials and Methods). We applied Deep-PALM to reconstruct an image set of labeled histone protein (H2B-PATagRFP) in human bone osteosarcoma (U2OS) cells using the networks trained on 4 and 6 emitters per μm^2 per frame (Materials and Methods). A varying number of predictions by the CNN of each individual frame of the input series were summed to reconstruct a temporal series of super resolved images (Supplementary Figure 1C). The predictions made by the CNN trained with 4 emitters per μm^2 show large spaces devoid of signal intensity, especially at the nuclear periphery, making this CNN inadequate for live-cell super-resolution imaging of chromatin. While collecting photons from long acquisitions for super-resolution imaging is desirable in fixed cells, Deep-PALM is a live imaging approach. Summing over many individual predictions leads to considerable motion blur and thus loss in resolution. Quantitatively, the Nyquist criterion states that the image resolution $R = 2/\sqrt{\tau\rho}$ depends on ρ, the localization density per second and the time resolution τ (*21*). In contrast, motion blur strictly depends on the diffusion constant D of the underlying structure $R = \sqrt{4D\tau}$. There is thus an optimum resolution due to the tradeoff between increased emitter sampling and the avoidance of motion blur, which was at a time resolution of 360 ms for our experiments (Figure 1B; Supplementary Figure 1D). Super-resolution imaging of H2B-PATagRFP in live cells at this temporal resolution shows a pronounced nuclear periphery while fluorescent signals in the interior vary in intensity (Figure 1C). This likely corresponds to chromatin-rich and chromatin-poor regions (*13*). These regions rearrange over time, reflecting the dynamic behavior of bulk chromatin. Chromatin-rich and chromatin-poor regions were visible not only at the scale of the whole-nucleus, but also at the resolution of a few hundred nanometers (Figure 1D). Within chromatin-rich regions, the intensity distribution was not uniform but exhibited spatially segregated accumulations of labeled histones of variable shape and size, reminiscent of nucleosome clutches (*10*), nanodomains (*14*, *16*) or TADs (*22*). At the nuclear periphery, prominent structures arise. Certain chromatin structures could be observed for ~ 1 s, which underwent conformational changes during this period

106 (Figure 1E). The spatial resolution at which structural elements can be observed (Materials and
107 Methods) in time-resolved super-resolution data of chromatin was 63 ± 2 nm (Figure 1E), slightly
108 more optimistic than the theoretical prediction (Figure 1B) (*23*). Thus, Deep-PALM identifies
109 spatially heterogeneous coverage of chromatin as previously reported (*10*, *13*, *14*, *16*, *22*). We
110 further monitor chromatin temporally at nanometer scale in living cells.
111

112 **Chromatin appears in elongated nanometer-sized blobs with a non-random spatial**
113 **distribution.**

114 To quantitatively assess the spatial distribution of H2B, we developed an image segmentation
115 scheme (Materials and Methods, Supplementary Figure 2) which allowed us to segment spatially
116 separated accumulations of H2B signal with high fidelity (Supplementary Note 1, Supplementary
117 Figure 3, Supplementary Figure 4). Applying our segmentation scheme, ~ 10,000 separable
118 elements, blob-like structures were observed for each super-resolved image (166 resolved images
119 per movie; Figure 2A). To elucidate their origin and formation, we used a transferable
120 computational model introduced by Qi *et al.* (*24*), which is based on one-dimensional genomics
121 and epigenomics data, including histone modification profiles and CTCF binding sites. Super-
122 resolution images were generated from the modeled chromosomes. Within these images we
123 identified and characterized 'chromatin blobs' analogously as for experimental data (Materials and
124 Methods; Figure 2B).

125 For both imaged and modeled chromatin, we first computed the kth nearest neighbor distance (NND;
126 centroid-to-centroid) distributions, taking into account the nearest 1st to 40th neighbors (Figure 2C,
127 blue to red). Centroids of nearest neighbors are (95 ± 30) nm (mean $\pm$ standard deviation) apart,
128 consistent with previous super-resolution images of chromatin in fixed cells (*14*) and slightly
129 further than what was found for clutches of nucleosomes (*10*). The envelope of all NND
130 distributions (Figure 2C, black line) shows several weak maxima at ~ 95 nm, 235 nm, 335 nm, and

450 nm, which roughly coincide with the peaks of the 1st, 7th, 14th and 25th nearest neighbors respectively (Figure 2C, red dots). In contrast, simulated data exhibit a prominent first nearest neighbor peak at slightly smaller distance and higher-order NND distribution decay quickly and appear washed out (Figure 2D). This hints towards greater levels of spatial organization of chromatin *in vivo*, which is not readily recapitulated in the employed state-of-the-art chromosome model.

Next, we were interested in the typical size of chromatin blobs. Their area distribution (Figure 2E) fit a log-normal distribution with parameters $(3.3 \pm 2.8) \cdot 10^{-3}$ μm^2 (mean $\pm$ standard deviation), which is in line with the area distribution derived from modeled chromosomes. Notably, blob areas vary considerably as indicated by the high standard deviation and the prominent tail of the area distribution towards large values. Following this we calculated the eccentricity of each blob to resolve their shape (Figure 2F). The eccentricity is a measure of the elongation of a region reflecting the ratio of the longest chord of the shape and the shortest chord perpendicular to it (Figure 2F, illustrated shapes at selected eccentricity values). The distribution of eccentricity values shows an accumulation of values close to 1, with a peak value of ~ 0.9, which shows that most blobs have an elongated, fiber-like shape and are not circular. In particular, the eccentricity value of 0.9 corresponds to a ratio between the short and long axis of the ellipse of ~ ½ (Materials and Methods), which results, considering the typical area of blobs, in roughly 92 nm long and 46 nm wide blobs on average. The length coincides with the value found for the typical nearest-neighbor distance (Figure 2C; (95 ± 30) nm). However, due to the segregation of chromatin into blobs, their elongated shape and their random orientation (Figure 2A), the blobs cannot be closely packed throughout the nucleus. We find that chromatin has a spatially heterogeneous density, occupying 5 - 60% of the nuclear area (Supplementary Figure 5A, B), which is supported by a previous electron microscopy study (*25*). The blob dimensions also fall within previously determined size ranges (*10*, *14*), confirming the existence of spatially segregated chromatin structures in the sub-100 nm range.

156 **Chromatin blobs identified by Deep-PALM are coherent with sub-TADs**

157 Due to the projection of the nuclear volume to the imaging plane, the observed blobs could simply
158 be overlays of distant, along the one-dimensional genome, non-interacting genomic loci. To
159 exclude this possibility, we analyzed the gap length along the simulated chromosome between
160 beads belonging to the same blob. The analysis showed that the blobs are mostly made of
161 consecutive beads along the genome, thus implying an underlying domain-like structure, similar to
162 TADs (Figure 3A). Using the affiliation of each bead to an intrinsic chromatin state of the model
163 (Figure 3B), it became apparent that blobs along the simulated chromosome consisting mostly of
164 active chromatin are significantly larger than those formed by inactive and repressive chromatin
165 (Figure 3C). These findings are in line with experimental results (*15*) and results from the
166 simulations directly (*24*), thereby validating the projection and segmentation process.

167 Since chromatin is dynamic *in vivo* and in computer simulations, each bead can diffuse in and
168 out of the imaging volume from frame to frame. We estimated that, on average, each bead spent
169 approximately 1.5 s continuously within a slab of 200 nm thickness (Figure 3D). Furthermore, a
170 bead is on average found only 0.55 ± 0.33 s continuously within a blob, which corresponds to 1 –
171 2 experimental super-resolved images (Figure 3D). These results suggest that chromatin blobs are
172 highly dynamic entities, which usually form and dissemble within less than one second. We thus
173 constructed a time-averaged association map for the modeled chromosomes, quantifying the
174 frequency at which each locus is found with any other locus within one blob. The association map
175 is comparable to interaction maps derived from Hi-C (Figure 3E). Strikingly, inter-loci association
176 and Hi-C maps are strongly correlated, and the association map shows similar patterns as those
177 identified as TADs in Hi-C maps, even for relatively distant genomic loci (> 1 Mbp). A similar
178 TAD-like organization is also apparent when the average inverse distance between loci is
179 considered (Figure 3F, upper panel), suggesting that blobs could be identified in super-resolved
180 images due to the proximity of loci within blobs in physical space. Using the computational

181 chromosome model, we conclude that chromatin blobs identified by Deep-PALM are mostly made
182 of continuous regions along the genome and cannot be attributed to artifacts originating from the
183 projection of the three-dimensional genome structure to the imaging plane. The blobs associate and
184 dissociate within less than one second, but loci within blobs are likely to belong to the same TAD.
185 Their average genomic content is 75 kb, only a fraction of typical TAD lengths in mammalian cells
186 (average size 880 kb) (*6*), suggesting that blobs likely correspond to sub-TADs or TAD nano-
187 compartments (*22*).
188

189 **Super-resolution chromatin dynamics using Deep-PALM**

190 To quantify the experimentally observed chromatin dynamics at the nanoscale, down to the size of
191 one pixel (13.5 nm), we used a dense reconstruction of flow fields, Optical Flow (OF; Figure 4A,
192 Materials and Methods), which was previously used to analyze images taken on confocal (*19*, *26*),
193 and Structured Illumination Microscopes (*13*). We examined the suitability of OF for super-
194 resolution based on single molecule localization images using simulations. We find that the
195 accuracy of OF is slightly enhanced on super-resolved images, compared to conventional
196 fluorescence microscopy images (Supplementary Note 2, Supplementary Figure 6). Experimental
197 super-resolution flow fields are illustrated on the basis of two subsequent images, between which
198 the dynamics of structural features are apparent to the eye (Figure 4B-C). On the nuclear periphery,
199 connected regions spanning up to ~ 500 nm can be observed (Figure 4B (i-ii), marked by arrows).
200 These structures are stable for at least 360 ms but move from frame to frame. The flow field is
201 shown on top of an overlay of the two super-resolve images and color-coded (Figure 4B (iii), the
202 intensity in frame 1 is shown in green, the intensity in frame one is shown in purple, co-localization
203 of both is white). Displacement vectors closely follow the redistribution of intensity from frame to
204 frame (roughly from green to purple). Similarly, structures within the nuclear interior (Figure 4C)

205 can be followed by eye, thus further validating and justifying the use of a dense motion
206 reconstruction as a quantification tool of super-resolved chromatin motion.
207 Using Optical Flow fields, we linked the spatial appearance of chromatin to their dynamics.
208 Effectively, the blobs were characterized with two structural parameters (NND and area) and their
209 flow magnitude (Figure 4D). Supplementary Movie 1 shows the time evolution of those parameters
210 for an exemplary nucleus. Blobs at the nuclear periphery showed a distinct behavior from those in
211 the nuclear interior. In particular, the periphery exhibits a lower density of blobs, but those appear
212 slightly larger and are less mobile than in the nuclear interior (Supplementary Figure 7), in line with
213 previous findings using conventional microscopy (*19*).
214

215 **Chromatin structure and dynamics are linked**

216 To further elucidate the relationship between chromatin structure and dynamics, we analyzed the
217 correlations between each pair of parameters in space and time. Therefore, we computed the auto-
218 and cross-correlation of parameter maps with a given time lag across the entire nucleus (in space)
219 (Figure 5A). In general, a positive correlation denotes a low-low or a high-high relationship (a
220 variable de-/increases when another variable de-/increases) while analogously a negative
221 correlation denotes a high-low relationship. The autocorrelation of NND maps (Figure 5A(i)) shows
222 a positive correlation, thus regions exist spanning 2 - 4 µm, in which chromatin is either closely
223 packed (low-low) or widely dispersed (high-high). Likewise, blobs of similar size tend to be in
224 spatial proximity (Figure 5A(iii)). These regions are not stable over time but rearrange
225 continuously, an observation bolstered by the fact that the autocorrelation diminishes with
226 increasing time lag. The cross-correlation between NND and area (Figure 5A(ii)) shows a negative
227 correlation for short time lags, suggesting that large blobs appear with a high local density while
228 small ones are more isolated. Interestingly, the correlation becomes slightly positive for time lags
229 ≥ 20 s, indicating that big blobs are present in regions which were sparsely populated before and

small blobs tend to accumulate in previously densely populated regions. This is in line with dynamic reorganization and reshaping of chromatin domains on a global scale as observed in snapshots of the Deep-PALM image series (Figure 1A).

The flow magnitude is positively correlated for all time lags, while the correlation displays a slight increase for time lags ≤ 20 s (Figure 5A(vi)), which has also been observed previously (*13*, *26*, *27*). The spatial autocorrelation of dynamic and structural properties of chromatin are in stark contrast. While structural parameters are highly correlated at short, but not at long time scales, chromatin motion is still correlated at a time scale exceeding 30 s. At very short time scales (< 100 ms), stochastic fluctuations determine the local motion of the chromatin fiber, while coherent motion becomes apparent at longer times (*27*). However, there exists a strong cross-correlation between structural and dynamic parameters: the cross-correlation between the NND and flow magnitude shows striking negative correlation at all time lags (Figure 5A(iv)), strongly suggesting that sparsely distributed blobs appear less mobile than densely packed ones. The area seems to play a negligible role for short time lags, but there is a modest tendency that regions with large blobs tend to exhibit increased dynamics at later time points (≥ 10 s; Figure 5A(v)), likely due to the strong relationship between area and NND.

In general, parameter pairs involving chromatin dynamics exhibit an extended spatial auto- or cross-correlation (up to ~ 6 µm; the lower row of Figure 5A), compared to correlation curves including solely structural parameters (up to 3 - 4 µm). Furthermore, the cross-correlation of flow magnitude and NND does not considerably change for increasing time lag, suggesting that the coupling between those parameters is characterized by a surprisingly resilient memory, lasting for at least tens of seconds (*28*). Concomitantly, the spatial correlation of time-averaged NND maps and maps of the local diffusion constant of chromatin for the entire acquisition time enforce their negative correlation at the time scale of ~ 1 min (Supplementary Figure 8). Such resilient memory was also proposed by a computational study that observed that interphase nuclei behave like concentrated

255 solutions of unentangled ring polymers (*29*). Our data support the view that chromatin is mostly
256 unentangled since entanglement would influence the anomalous exponent of genomic loci in
257 regions of varying chromatin density (*29*, *30*). However, our data do not reveal a correlation
258 between the anomalous exponent and the time-averaged chromatin density (Supplementary Figure
259 8), in line with our previous results using conventional microscopy (*19*).
260 Overall, the spatial cross-correlation between chromatin structure and dynamics indicates that the
261 NND between blobs and their mobility stand in a strong mutual, negative, relationship. This
262 relationship, however, concerns chromatin density variations at the nanoscale, but not global spatial
263 density variations such as in eu- or heterochromatin (*19*). These results support a model in which
264 regions with high local chromatin density, larger blobs are more prevalent and are mobile, while
265 small blobs are sparsely distributed and less mobile (Figure 5B). Blob density and dynamics in the
266 long-time limit are to a surprisingly large extent influenced by preceding chromatin conformations.
267

268 **The local chromatin density is a key regulator of instantaneous chromatin dynamics**

269 The spatial correlations above were only evaluated pairwise, while the behavior of every blob is
270 likely determined by a multitude of factors in the complex energy landscape of chromatin (*24*, *27*).
271 Here, we aim to take a wider range of available information into account in order to reveal the
272 principle parameters, driving the observed chromatin structure and dynamics. Employing a
273 microscopy-based approach, we have access to a total of six relevant structural, dynamic and global
274 parameters, which potentially shape the chromatin landscape in space and time (Figure 6A). In
275 addition to the parameters used above, we included the confinement level as a relative measure,
276 allowing the quantification of transient confinement (Materials and Methods). We further included
277 the bare signal intensity of super-resolved images and, as the only static parameter, the distance
278 from the periphery since it was shown that dynamic and structural parameters show some
279 dependence on this parameter (Supplementary Figure 7). We then employed t-Distributed

Stochastic Neighbor Embedding (*31*) (t-SNE), a state of the art dimensionality reduction technique, to map the six-dimensional chromatin 'features' (the six input parameters) into two dimensions. (Figure 6A, see Supplementary Note 3). The t-SNE algorithm projects data points such that neighbors in high-dimensional space likely stay neighbors in two-dimensional space (*31*). Visually apparent grouping of points (Figure 6B) implies that grouped points exhibit great similarity with respect to all input features and it is of interest to reveal which subset of the input features can explain the similarity among chromatin blobs best. It is likely that points appear grouped because their value of a certain input feature is considerably higher or lower than the corresponding value of other data points. We hence labeled points in t-SNE maps which are smaller than the first quartile point or larger than the third quartile point. Data points falling in either of the low/high partition of one input feature are colored accordingly for visualization (Figure 6D; blue/red points respectively). We then assigned a rank to each of the input features according to their nearest-neighbor fraction (n-n fraction): Since the t-SNE algorithm conserves nearest neighbors, we described the extent of grouping in t-SNE maps by the fraction of nearest neighbors which fall in either one of the subpopulations of low or high points (illustrated in Supplementary Figure 9). A high nearest neighbor fraction (n-n fraction; Figure 6C) therefore indicates that many points marked as low/high are indeed grouped by t-SNE and are therefore similar. The ranking (from low to high n-n fraction) reflects the potency of a given parameter to induce similar behavior between chromatin blobs with respect to all input features.

The relative frequency at which each parameter ranked first provides an intuitive feeling for the most 'influential' parameters in the dataset (Figure 6E). The signal intensity plays a negligible role, suggesting that our data is free of potential artifacts related to the bare signal intensity. Furthermore, the blob area and the distance from the periphery likewise do not considerably shape chromatin blobs. In contrast, the NND between blobs was found to be the main factor inducing the observed characteristics in 67 % of all-time frames across all nuclei. The flow magnitude and confinement

305 level together rank 1st in 26 % of all cases (11 % and 17 %, respectively). These numbers suggest
306 that the local chromatin density is a universal key regulator of instantaneous chromatin dynamics.
307 Note that no temporal dependency is included in the t-SNE analysis and thus the feature extraction
308 concerns only short-term (≤ 360 ms) relationships. The characteristics of roughly one-fourth of all
309 blobs at each time point are mainly determined by similar dynamical features. Mapping chromatin
310 blobs as marked in Figure 6C, D back to their respective positions inside the nucleus (Figure 6F)
311 shows that blobs with low/high flow magnitude or confinement level markedly also grouped in
312 physical space, which is highly reminiscent of coherent motion of chromatin (*26*). In contrast, blobs
313 with extraordinary low or high NND were found interspersed throughout the nucleus, in line with
314 spatial correlation analysis between structural and dynamic features (Figure 5). Our results point
315 towards a large influence of the local chromatin density on the dynamics of chromatin at the scale
316 of a few hundred nanometers and within a few hundred milliseconds. At longer time and length
317 scales, however, previous results suggest that this relationship is lost (*19*)
318

319 **Discussion**

320 With Deep-PALM we present temporally resolved super-resolution images of chromatin in living
321 cells. Our technique identified chromatin nanodomains, called "blobs", which mostly have an
322 elongated shape, consistent with the curvilinear arrangement of chromatin as revealed by Structured
323 Illumination Microscopy (*13*) with typical axes length of 45 – 90 nm. A previous study reported
324 ~30 nm wide 'clutches of nucleosomes' in fixed mammalian cells using STORM nanoscopy (*10*),
325 while the larger value obtained using Deep-PALM may be attributed to the motion blurring effect
326 in live-cell imaging. However, histone acetylation and methylation marks were shown to form
327 nanodomains of diameter 60 – 140 nm, respectively (*14*), which includes the computed dimensions
328 for histone H2B using Deep-PALM.

329 Using an established chromosome model, chromatin blobs were shown to consist of continuous
330 genomic regions with an average length of 75 kb. While assembling and disassembling dynamically
331 within less than one second. Monomers within blobs display a distinct TAD-like association pattern
332 in the long-time limit, suggesting that the identified blobs represent sub-TADs. Transient formation
333 is consistent with recent findings that TADs are not stable structural elements, but exhibit extensive
334 heterogeneity and dynamics (*7*, *9*).
335 We found that structural and dynamic parameters exhibit extended spatial and temporal (cross-)
336 correlations. Structural parameters such as the local chromatin density (expressed as the NND
337 between blobs) and area lose their correlation after 3 – 4 μm and roughly 40 s in the spatial and
338 temporal dimension, respectively. In contrast, chromatin mobility correlations extend over ~ 6 μm
339 and persist during the whole acquisition period (≥ 40 s). Extensive spatio-temporal correlation of
340 chromatin dynamics have been presented previously, both experimentally (*26*) and in simulations
341 (*27*), but was not linked to the spatio-temporal behavior of the underlying chromatin structure until
342 now. We found that the chromatin dynamics are closely linked to the instantaneous, but also to past
343 local structural characterization of chromatin. In other words, the instantaneous local chromatin
344 density influences chromatin dynamics in the future and vice versa. Based on these findings, we
345 suggest that chromatin dynamics exhibit an extraordinary long memory. This strong temporal
346 relationship might be established by the fact that stress propagation is affected by the folded
347 chromosome organization (*32*). Fiber displacements cause structural reconfiguration, ultimately
348 leading to a local amplification of chromatin motion in local high-density environments. This
349 observation is also supported by the fact that increased nucleosome mobility grants chromatin
350 accessibility even within regions of high nucleosome density (*33*).
351 Given the persistence at which correlations of chromatin structure and, foremost, dynamics occur
352 in a spatio-temporal manner, we speculate that the interplay of chromatin structure and dynamics
353 could involve a functional relationship (*34*): transcriptional activity is closely linked to chromatin

accessibility and the epigenomic state (*35*). Because chromatin structure and dynamics are related, dynamics could also correlate with transcriptional activity (*19*, *36*). However, it is currently unknown if the structure-dynamics relationship revealed here is strictly mutual or if it may be causal. Simulations hint that chromatin dynamics follows from structure (*27*, *28*), this question will be exciting to answer experimentally and in the light of active chromatin remodelers in order to elucidate a potential functional relationship to transcription. Chromatin regions which are switched from inactive to actively transcribing, for instance, undergo a structural reorganization accompanied by epigenetic modifications (*37*, *38*). The mechanisms driving recruitment of enzymes inducing histone modifications such as histone acetyltransferases, deacetylases or methyltransferases is largely unknown, but often involves the association to proteins (*39*). Their accessibility to the chromatin fiber is inter alia determined by local dynamics (*33*). Such a structure-dynamics feedback loop would constitute a quick and flexible way to transiently alter gene expression patterns upon reaction to external stimuli or to co-regulate distant genes (*40*). Future work will study how structure-dynamics correlations differ in regions of different transcriptional activity and/or epigenomic states. Furthermore, to probe the interactions between key transcriptional machines such as RNA polymerases with the local chromatin structure and to record their (possibly collective) dynamics could shed light into the target search and binding mechanisms of RNA polymerases with respect to the local chromatin structure. Deep-PALM in combination with Optical Flow paves the way to answer these questions by enabling the analysis of time-resolved super-resolution images of chromatin in living cells.

379 **Materials and Methods**

380 **Cell Culture.**

381 Human osteosarcoma U2OS expressing H2B-PATagRFP cells were a gift from Sébastien Huet
382 (CNRS, UMR 6290, Institut Génétique et Développement de Rennes, Rennes, France); the histone
383 H2B was cloned as described previously (*41*). U2OS cells were cultured in DMEM (with 4.5 g/l
384 glucose) supplemented with 10% fetal bovine serum (FBS), 2 mM glutamine, 100 µg/ml penicillin,
385 and 100 U/ml streptomycin in 5% CO_2 at 37°C. Cells were plated 24 hours before imaging on 35
386 mm Petri dishes with a #1.5 coverslip like bottom (ibidi, Biovalley) with a density of 2×10^5
387 cells/dish. Just before imaging, the growth medium was replaced by Leibovitz's L-15 medium (Life
388 Technologies) supplemented with 20% FBS, 2 mM glutamine, 100 µg/ml penicillin, and 100 U/ml
389 streptomycin.

390

391 **PALM Imaging.**

392 Imaging of H2B-PAtagRFP in live U2OS cells was carried out on a fully automated Nikon TI-E/B
393 PALM (Nikon Instruments) microscope. The microscope is equipped with a full incubator
394 enclosure with gas regulation to maintain a temperature of ~37°C for normal cell growth during
395 live-cell imaging. A laser line of 561 nm (~50-60 W/cm^2 at the sample) was applied for PATagRFP
396 excitation and the 405 nm laser used for photo-activation (~2-2.5 W/cm^2 at the sample). Laser beam
397 powers were controlled by acoustic optic-modulators (AA Opto-Electronics). Both wavelengths
398 were united into an oil immersion 1.49 NA TIRF objective (100x; Nikon). An oblique illumination
399 was applied to acquire image series with high signal to noise ratio. The fluorescence emission signal
400 was collected by using the same objective and spectrally filtered by a Quad-Band beam splitter
401 (ZT405/488/561/647rpc-UF2, Chroma Technology) with Quad-Band emission filter
402 (ZET405/488/561/647m-TRF, Chroma). The signal was recorded on an EMCCD camera (Andor
403 iXon X3 DU-897, Andor Technologies) with a pixel size of 108 nm. For axial correction, Perfect

Focus System was applied to correct for defocusing. NIS-Elements software was used for acquiring the images at 30 ms per frame.

Deep-PALM analysis. The convolutional neural network (CNN) was trained using simulated data following Nehme *et al.* (*20*) for three labeling densities (4, 6 and 9 emitters per μm^2 per frame). Raw imaging data were checked for drift as previously described (*26*). The detected drift in raw images is in the range < 10 nm and therefore negligible. The accuracy of the trained net was evaluated by constructing ground truth images from the simulated emitter positions. The Structural Similarity Index is computed to assess the similarity between reconstructed and ground truth images (*42*):

$$SSIM = \sum_{x,y} \frac{(2\mu_x\mu_x + C_1)(2\sigma_{xy} + C_2)}{(\mu_x^2 + \mu_y^2 + C_1)(\sigma_x^2 + \sigma_y^2 + C_2)}, \quad (1)$$

where x and y are windows of the predicted and ground truth images, respectively, μ and σ denote their local means and standard deviation, respectively and σ_{xy} their cross-variance. $C_1 = (0.01L)^2$ and $C_2 = (0.03L)^2$ are regularization constants, where L is the dynamic range of the input images. The second quantity to assess CNN accuracy is the Root Mean Square Error between the ground truth G and reconstructed image R:

$$RMSE = \sqrt{\frac{1}{N}\sum_{N}(R - G)^2}, \quad (2)$$

Where N is the number of pixels in the images. After training, experimental data were supplied to the trained network and predictions of single Deep-PALM images were summed to a final super-resolved image. An up-sampling factor of 8 was used, resulting in an effective pixel size of $108\ \mathrm{nm}/8 = 13.5\ \mathrm{nm}$. The image quality assessment in order to determine the optimal number of predictions to be summed, we use a blind/referenceless image spatial quality evaluator (BRISQUE)

426 (*43*). For visualization, super-resolved images were convolved with a Gaussian kernel ($\sigma = 1$
427 pixel) and represented using a false RGB colormap.
428
429 **Fourier Ring Correlation analysis.** Fourier Ring Correlation (FRC) is an unbiased method to
430 estimate the spatial resolution in microscopy images. We follow an approach similar to the one
431 described in Nieuwenhuizen *et al.* (*44*). For localization-based super-resolution techniques, the set
432 of localizations is divided into two statistically independent subsets and two images from these
433 subsets are generated. The FRC is computed as the statistical correlation of the Fourier transforms
434 of both sub-images over the perimeter of circles of constant frequency in the frequency domain.
435 Deep-PALM, however, does not result in a list of localizations, but in predicted images directly.
436 The set of 12 predictions from Deep-PALM were thus split into two statistically independent
437 subsets and the method described in Nieuwenhuizen *et al.* (*44*) was applied.
438
439 **Chromatin blob identification.** The super-resolved images displayed isolated regions of
440 accumulated emitter density. To quantitatively assess the structural information implied by these
441 accumulation of emitters in the focal plane, we developed a segmentation scheme which aims to
442 identify individual blobs (Supplementary Figure 2). A marker-assisted watershed segmentation was
443 adapted in order to accurately determine blob boundaries. For this purpose, we use the raw
444 predictions from the deep convolutional neural network without convolution (Supplementary
445 Figure 2A). The foreground in this image is marked by regional maxima and pixels with very high
446 density (i.e. those with $I > 0.99\, I_{max}$, Supplementary Figure 2B). Since blobs are characterized by
447 surrounding pixels of considerably less density, the Euclidian distance transform is computed on
448 the binary foreground markers. Background pixels (i.e. those pixels not belonging to any blobs) are
449 expected to lie far away from any blob center and thus, a good estimate for background markers are
450 those pixels being furthest from any foreground pixel. We hence compute the watershed transform

on the distance transform of foreground markers and the resulting watershed lines depict background pixels (Supplementary Figure 2C). Equipped with fore- and background markers (Supplementary Figure 2D), we apply a marker-controlled watershed transform on the gradient of the input image (Supplementary Figure 2E). The marker-controlled watershed imposes minima on marker pixels preventing the formation of watershed lines across marker pixels. Therefore, the marker-controlled watershed accurately detects boundaries as well as blobs which might not have been previously marked as foreground (Supplementary Figure 2F). Finally, spurious blobs whose median- or mean intensity is below 10% of the maximum intensity are discarded and each blob is assigned a unique label for further correspondence (Supplementary Figure 2G). The area and centroid position are computed for each identified blob for further analysis. This automated segmentation scheme performs considerably better than other state-of-the-art algorithms for image segmentation due to the reliable identification of fore- and background markers accompanied by the watershed transform (Supplementary Note 1).

Chromatin blob properties. Centroid position, area, and eccentricity were computed. The eccentricity is computed by describing the blobs as an ellipse:

$$E = \sqrt{1 - a^2/b^2} \tag{3}$$

where a and b are the short and long axes of the ellipse, respectively.

Chromatin blob identification from a computational chromatin model. We chose to employ a computational chromatin model, recently introduced by Qi *et al.* (*24*), in order to elucidate the origin of experimentally determined chromatin blobs. Each bead of the model covers a sequence length of 5 kb and is assigned one of 15 chromatin states to distinguish promoters, enhancers, quiescent chromatin, etc. Starting from the simulated polymer configurations, we consider monomers within a 200 nm thick slab through the center of the simulated chromosome. In order to

475 generate super-resolved images as those from Deep-PALM analysis, fluorescence intensity is
476 ascribed to each monomer. Monomer positions are subsequently discretized on a grid with 13.5 nm
477 spacing and convolved with a narrow point-spread function, which results in images closely
478 resembling experimental Deep-PALM images of chromatin. Chromatin blobs were then be
479 identified and characterized as on experimental data (Figure 2A, B). Mapping back the association
480 of each bead to a blob (if any) allows us to analyze principles of blob formation and maintenance
481 using the distance and the association strength between each pair of monomers, averaged over all
482 20,000 simulated polymer configurations.
483
484 **Radial distribution function.** The radial distribution function $g(r)$ (RDF, also pair correlation
485 function) is calculated (in two dimensions) by counting the number of blobs in an annulus of radius
486 r and thickness dr. The result is normalized by the bulk density $\rho = n/A$, with the total number of
487 blobs n and A the area of the nucleus, and the area of the annulus, $2\pi r\, dr$:

$$dn(r) = \rho \cdot g(r) \cdot 2\pi r\, dr \quad (4)$$

488 **Quantification of chromatin dynamics.** Super-resolved images of chromatin showed spatially
489 distributed blobs of varying size, but the resolved structure is too dense for state-of-the-art single
490 particle tracking methods to track. Furthermore, are highly dynamic structures, assembling and
491 dissembling within 1 – 2 super-resolved frames (Figure 3D), which makes a Single Particle
492 Tracking approach unsuitable. Instead, we used a method for dynamics reconstruction of bulk
493 macromolecules with dense labeling, Optical Flow. Optical Flow builds upon the computation of
494 flow fields between two successive frames of an image series. The integration of these flow fields
495 from super-resolution images results in trajectories displaying the local motion of bulk chromatin
496 with temporal and high spatial resolution. Further, the trajectories are classified into various
497 diffusion models and parameters describing the underlying motion are computed (*19*). Here, we use
498 the effective diffusion coefficient D (in units of m^2/s^α), which reflects the magnitude of
499 displacements between successive frames (the velocity of particles or monomers in the continuous

limit) and the anomalous exponent α (*19*). The anomalous exponent reflects if the diffusion is free ($\alpha = 1$, e.g. for non-interacting particles in solution), directed ($\alpha > 1$, e.g. as the result from active processes) or hindered ($\alpha < 1$, e.g. due to obstacles or an effective back-driving force). Furthermore, we compute the length of constraint L_c which is defined as the standard deviation of the trajectory positions with respect to its time-averaged position. Denoting $\boldsymbol{R}(t; \boldsymbol{R_0})$ the trajectory at time t originating from $\boldsymbol{R_0}$, the expression reads (*45*) $L_c(\boldsymbol{R_0}) = var\big(\boldsymbol{R}(t; \boldsymbol{R_0})\big)^{1/2}$, where var denotes the variance. The length of constraint is a measure of the length scale explored of the monomer during the observation period. A complementary measure is the confinement level (*46*), which computes the inverse of the variance of displacements within a sliding window of length ω: $C \propto \omega/\mathrm{var}\big(\boldsymbol{R}(t; \boldsymbol{R_0})\big)$, where the sliding window length is set to 4 frames (1.44 s). Larger values of C denote a more confined state than small ones.

Spatial correlation for temporally varying parameters. The nearest-neighbor distance and the area, as well as the flow magnitude, were calculated and assigned to the blobs' centroid position. In order to calculate the spatial correlation between parameters, the parameters were interpolated from the scattered centroid positions onto a regular grid spanning the entire nucleus. Because not every pixel in the original super-resolved images is assigned a parameter value, we chose an effective grid spacing of 5 pixels (67.5 nm) for the interpolated parameter maps. After interpolation, the spatial correlation was computed between parameter pairs: Let $\boldsymbol{r} = (x, y)^T$ denote a position on a regular two-dimensional grid and $f(\boldsymbol{r}, t)$ and $g(\boldsymbol{r}, t)$ two scalar fields with mean zero and variance one, at time t on that grid. The time series of parameter fields consist of N time points. The spatial cross-correlation between the fields f and g, which lie a lag time τ apart, is then calculated as

$$C(\boldsymbol{\rho},\tau) = \frac{1}{N}\sum_{t}\frac{\sum_{x,y} f(\boldsymbol{r},t)g(\boldsymbol{r}+\boldsymbol{\rho},t+\tau)}{\sum_{x,y} f(\boldsymbol{r},t)\cdot g(\boldsymbol{r},t+\tau)} \quad (5)$$

where the space lag $\boldsymbol{\rho}$ is a two-dimensional vector $\boldsymbol{\rho} = (\Delta x, \Delta y)^T$. The sums in the numerator and denominator are taken over the spatial dimensions, the first sum is taken over time. The average is thus taken over all time points which are compliant with time lag τ. Subsequently, the radial average in space is taken over the correlation, thus effectively calculating the spatial correlation $C(\rho,\tau)$ over the space lag $\rho = \sqrt{\Delta x^2 + \Delta y^2}$. If $f = g$, the spatial autocorrelation is computed.

Spatial correlation for static parameters. We denote global parameters as those, which reflect the structural and dynamic behavior of chromatin spatially resolved, but in a time-averaged manner. Examples involve the diffusion constant, the anomalous exponent, the length of constraint, but also time-averaged nearest-neighbor distance maps, etc. (Supplementary Figure 8). Those parameters are useful to determine time-universal characteristics. The spatial correlation between those parameters is equivalent to the expression given for temporally varying parameters when the temporal dimension is omitted, effectively resulting in a correlation curve $C(\rho)$.

t-Distributed Stochastic Neighbor Embedding (t-SNE). The distance from the periphery, intensity, their nearest-neighbor distance, area, flow magnitude and confinement level of each identified blob form the six-dimensional input feature space for t-SNE analysis. The parameters for each blob (n = 3,260,232, divided into subsets of approximately 10,000) were z-transformed prior to the t-SNE analysis. The t-SNE analysis was performed using MATLAB and the Statistics and Machine Learning Toolbox (Release 2017b, The MathWorks, Inc., Natick, Massachusetts, United States) with the Barnes-Hut approximation. The algorithm was tested using different distance metrics and perplexity values and showed robust results within the examined ranges (Supplementary Note 3, Supplementary Figure 10).

547 **H2: Supplementary Materials**

548

549 Note S1. Performance of the segmentation scheme employed for this study in comparison to other
550 state-of-the-art algorithms for general purpose and comparison of blob segmentation on
551 experimental images and on images containing randomly distributed emitters.

552 Note S2. Suitability of Optical Flow for super-resolution images of chromatin.

553 Note S3. t-SNE and its robustness with respect to distance metrics and perplexity values.

554 Figure S1. CNN training and time-resolution determination.

555 Figure S2. Chromatin blob identification pipeline.

556 Figure S3. Performance of segmentation algorithms on super-resolved images of chromatin *in vivo*.

557 Figure S4. Segmentation on images of randomly distributed emitters.

558 Figure S5. Chromatin area fraction.

559 Figure S6. Performance of Optical Flow on conventional and super-resolved images.

560 Figure S7. Structural and dynamic parameters are dependent on the proximity to the nuclear
561 periphery.

562 Figure S8. Global spatial correlation of structural and dynamic parameters.

563 Figure S9. Clustering illustration of points within a subset based on nearest-neighbors in t-SNE
564 maps.

565 Figure S10. t-SNE for different distance metrics and perplexity values.

566 Movie S1. Time series of super-resolved chromatin structure and dynamics.

567

568 **References and Notes**

569 1. J. H. Gibcus, J. Dekker, The Hierarchy of the 3D Genome. *Mol. Cell*. **49** (2013), pp. 773–
570 782.

571 2. W. A. Bickmore, The spatial organization of the human genome. *Annu Rev Genomics Hum*

572 *Genet*. **14**, 67–84 (2013).

573 3. B. van Steensel, E. E. M. Furlong, The role of transcription in shaping the spatial
574 organization of the genome. *Nat. Rev. Mol. Cell Biol.* (2019), , doi:10.1038/s41580-019-
575 0114-6.

576 4. E. Lieberman-Aiden, N. L. van Berkum, L. Williams, M. Imakaev, T. Ragoczy, A. Telling,
577 I. Amit, B. R. Lajoie, P. J. Sabo, M. O. Dorschner, R. Sandstrom, B. Bernstein, M. A.
578 Bender, M. Groudine, A. Gnirke, J. Stamatoyannopoulos, L. A. Mirny, E. S. Lander, J.
579 Dekker, N. L. Van Berkum, L. Williams, M. Imakaev, T. Ragoczy, A. Telling, I. Amit, B.
580 R. Lajoie, P. J. Sabo, M. O. Dorschner, R. Sandstrom, B. Bernstein, M. A. Bender, M.
581 Groudine, A. Gnirke, J. Stamatoyannopoulos, L. A. Mirny, Comprehensive Mapping of
582 Long-Range Interactions Reveals Folding Principles of the Human Genome. *Science (80-.*
583 *).* **326**, 289–293 (2009).

584 5. A. Bolzer, G. Kreth, I. Solovei, D. Koehler, K. Saracoglu, C. Fauth, S. M??ller, R. Eils, C.
585 Cremer, M. R. Speicher, T. Cremer, Three-dimensional maps of all chromosomes in
586 human male fibroblast nuclei and prometaphase rosettes. *PLoS Biol.* **3**, 0826–0842 (2005).

587 6. J. R. Dixon, S. Selvaraj, F. Yue, A. Kim, Y. Li, Y. Shen, M. Hu, J. S. Liu, B. Ren,
588 Topological domains in mammalian genomes identified by analysis of chromatin
589 interactions. *Nature*. **485**, 376–380 (2012).

590 7. B. Bintu, L. J. Mateo, J.-H. Su, N. A. Sinnott-Armstrong, M. Parker, S. Kinrot, K. Yamaya,
591 A. N. Boettiger, X. Zhuang, Super-resolution chromatin tracing reveals domains and
592 cooperative interactions in single cells. *Science (80-.).* **362**, eaau1783 (2018).

593 8. M. Spielmann, D. G. Lupiáñez, S. Mundlos, Structural variation in the 3D genome. *Nat.*
594 *Rev. Genet.* **19**, 453–467 (2018).

595 9. E. H. Finn, G. Pegoraro, H. B. Brandão, A. L. Valton, M. E. Oomen, J. Dekker, L. Mirny,
596 T. Misteli, Extensive Heterogeneity and Intrinsic Variation in Spatial Genome

597 Organization. *Cell*. **176**, 1502-1515.e10 (2019).

598 10. M. A. Ricci, C. Manzo, M. F. García-Parajo, M. Lakadamyali, M. P. Cosma, Chromatin
599 fibers are formed by heterogeneous groups of nucleosomes in vivo. *Cell* (2015),
600 doi:10.1016/j.cell.2015.01.054.

601 11. B. Dong, L. M. Almassalha, Y. Stypula-Cyru, B. E. Urban, J. E. Chandler, T. Q. Nguyen,
602 C. Sun, H. F. Zhang, V. Backman, Superresolution intrinsic fluorescence imaging of
603 chromatin utilizing native, unmodified nucleic acids for contrast. *Proc. Natl. Acad. Sci. U.*
604 *S. A.* (2016), doi:10.1073/pnas.1602202113.

605 12. K. Fang, X. Chen, X. Li, Y. Shen, J. Sun, D. M. Czajkowsky, Z. Shao, Super-resolution
606 Imaging of Individual Human Subchromosomal Regions in Situ Reveals Nanoscopic
607 Building Blocks of Higher-Order Structure. *ACS Nano* (2018),
608 doi:10.1021/acsnano.8b01963.

609 13. E. Miron, R. Oldenkamp, D. M. S. Pinto, J. M. Brown, A. R. Faria, H. A. Shaban, J. D. P.
610 Rhodes, C. Innocent, S. de Ornellas, V. Buckle, L. Schermelleh, Chromatin arranges in
611 filaments of blobs with nanoscale functional zonation. *bioRxiv*, 566638 (2019).

612 14. J. Xu, H. Ma, J. Jin, S. Uttam, R. Fu, Y. Huang, Y. Liu, H. Ma, J. Jin, S. Uttam, R. Fu, Y.
613 Huang, Y. Liu, Super-Resolution Imaging of Higher-Order Chromatin Structures at
614 Different Epigenomic States in Single Mammalian Cells. *Cell Rep.* **24** (2018),
615 doi:10.1016/j.celrep.2018.06.085.

616 15. A. N. Boettiger, B. Bintu, J. R. Moffitt, S. Wang, B. J. Beliveau, G. Fudenberg, M.
617 Imakaev, L. A. Mirny, C. T. Wu, X. Zhuang, Super-resolution imaging reveals distinct
618 chromatin folding for different epigenetic states. *Nature*. **529**, 418–422 (2016).

619 16. T. Nozaki, R. Imai, M. Tanbo, R. Nagashima, S. Tamura, T. Tani, Y. Joti, M. Tomita, K.
620 Hibino, M. T. Kanemaki, K. S. Wendt, Y. Okada, T. Nagai, K. Maeshima, Dynamic
621 Organization of Chromatin Domains Revealed by Super-Resolution Live-Cell Imaging.

622 *Mol. Cell*. **67**, 282-293.e7 (2017).

623 17. H. A. Shaban, R. Barth, K. Bystricky, Formation of correlated chromatin domains at
624 nanoscale dynamic resolution during transcription. *Nucleic Acids Res.* **46**, e77–e77 (2018).

625 18. W. Xiang, M. J. Roberti, J.-K. Hériché, S. Huet, S. Alexander, J. Ellenberg, Correlative
626 live and super-resolution imaging reveals the dynamic structure of replication domains. *J.*
627 *Cell Biol.* **217**, 1973–1984 (2018).

628 19. H. A. Shaban, R. Barth, K. Bystricky, Nanoscale mapping of DNA dynamics in live human
629 cells. *Bioarxiv* (2018).

630 20. E. Nehme, L. E. Weiss, T. Michaeli, Y. Shechtman, Deep-STORM: super-resolution
631 single-molecule microscopy by deep learning. *Optica*. **5**, 458 (2018).

632 21. H. Shroff, C. G. Galbraith, J. A. Galbraith, E. Betzig, Live-cell photoactivated localization
633 microscopy of nanoscale adhesion dynamics. *Nat. Methods* (2008),
634 doi:10.1038/nmeth.1202.

635 22. Q. Szabo, D. Jost, J.-M. M. Chang, D. I. Cattoni, G. L. Papadopoulos, B. Bonev, T. Sexton,
636 J. Gurgo, C. Jacquier, M. Nollmann, F. Bantignies, G. Cavalli, G. L. Papadopoulos, Q.
637 Szabo, B. Bonev, D. Jost, F. Bantignies, C. Jacquier, D. I. Cattoni, J. Gurgo, M. Nollmann,
638 J.-M. M. Chang, G. Cavalli, TADs are 3D structural units of higher-order chromosome
639 organization in Drosophila . *Sci. Adv.* **4**, eaar8082 (2018).

640 23. R. J. Marsh, K. Pfisterer, P. Bennett, L. M. Hirvonen, M. Gautel, G. E. Jones, S. Cox,
641 Artifact-free high-density localization microscopy analysis. *Nat. Methods*. **15**, 689–692
642 (2018).

643 24. Y. Qi, B. Zhang, Predicting three-dimensional genome organization with chromatin states.
644 *PLOS Comput. Biol.* **15**, e1007024 (2019).

645 25. H. D. Ou, S. Phan, T. J. Deerinck, A. Thor, M. H. Ellisman, C. C. O'Shea, ChromEMT:
646 Visualizing 3D chromatin structure and compaction in interphase and mitotic cells. *Science*

647 *(80-.).* **357** (2017), doi:10.1126/science.aag0025.

648 26. H. A. Shaban, R. Barth, K. Bystricky, Formation of correlated chromatin domains at
649 nanoscale dynamic resolution during transcription. *Nucleic Acids Res.* **46**, e77–e77 (2018).

650 27. M. Di Pierro, D. A. Potoyan, P. G. Wolynes, J. N. Onuchic, Anomalous diffusion, spatial
651 coherence, and viscoelasticity from the energy landscape of human chromosomes. *Proc.*
652 *Natl. Acad. Sci.* **115**, 7753–7758 (2018).

653 28. L. Liu, G. Shi, D. Thirumalai, C. Hyeon, Chain organization of human interphase
654 chromosome determines the spatiotemporal dynamics of chromatin loci. *PLOS Comput.*
655 *Biol.* **14**, e1006617 (2018).

656 29. A. Rosa, R. Everaers, Structure and Dynamics of Interphase Chromosomes. *PLoS Comput.*
657 *Biol.* **4**, e1000153 (2008).

658 30. P. G. de Gennes, L. Leger, Dynamics of Entangled Polymer Chains. *Annu. Rev. Phys.*
659 *Chem.* **33**, 49–61 (1982).

660 31. L. Van Der Maaten, G. Hinton, Visualizing Data using t-SNE. **9**, 2579–2605 (2008).

661 32. K. E. Polovnikov, M. Gherardi, M. Cosentino-Lagomarsino, M. V. Tamm, Fractal Folding
662 and Medium Viscoelasticity Contribute Jointly to Chromosome Dynamics. *Phys. Rev. Lett.*
663 **120**, 88101 (2018).

664 33. S. Hihara, C.-G. G. Pack, K. Kaizu, T. Tani, T. Hanafusa, T. Nozaki, S. Takemoto, T.
665 Yoshimi, H. Yokota, N. Imamoto, Y. Sako, M. Kinjo, K. Takahashi, T. Nagai, K.
666 Maeshima, Local Nucleosome Dynamics Facilitate Chromatin Accessibility in Living
667 Mammalian Cells. *Cell Rep.* **2**, 1645–1656 (2012).

668 34. L. Giorgetti, R. Galupa, E. P. Nora, T. Piolot, F. Lam, J. Dekker, G. Tiana, E. Heard,
669 Predictive polymer modeling reveals coupled fluctuations in chromosome conformation
670 and transcription. *Cell*. **157**, 950–963 (2014).

671 35. S. M. Gorisch, Histone acetylation increases chromatin accessibility. *J. Cell Sci.* **118**,

672 5825–5834 (2005).
673 36. T. Germier, S. Kocanova, N. Walther, A. Bancaud, H. A. Shaban, H. Sellou, A. Z. Politi, J.
674 Ellenberg, F. Gallardo, K. Bystricky, Real-Time Imaging of a Single Gene Reveals
675 Transcription-Initiated Local Confinement. *Biophys. J.* **113**, 1383–1394 (2017).
676 37. N. Soshnikova, D. Duboule, Epigenetic Temporal Control of Mouse Hox Genes in Vivo.
677 *Science (80-.).* **324**, 1320–1323 (2009).
678 38. D. Noordermeer, M. Leleu, E. Splinter, J. Rougemont, W. De Laat, D. Duboule, The
679 Dynamic Architecture of Hox Gene Clusters. *Science (80-.).* **334**, 222–225 (2011).
680 39. M. Laisné, N. Gupta, O. Kirsh, S. Pradhan, P.-A. Defossez, Mechanisms of DNA
681 Methyltransferase Recruitment in Mammals. *Genes (Basel).* **9**, 617 (2018).
682 40. P. Fraser, W. Bickmore, Nuclear organization of the genome and the potential for gene
683 regulation. *Nature*. **447**, 413–417 (2007).
684 41. H. Sellou, T. Lebeaupin, C. Chapuis, R. Smith, A. Hegele, H. R. Singh, M. Kozlowski, S.
685 Bultmann, A. G. Ladurner, G. Timinszky, S. Huet, The poly(ADP-ribose)-dependent
686 chromatin remodeler Alc1 induces local chromatin relaxation upon DNA damage. *Mol.*
687 *Biol. Cell*. **27**, 3791–3799 (2016).
688 42. Z. Wang, A. C. Bovik, H. R. Sheikh, E. P. Simoncelli, Image quality assessment: From
689 error visibility to structural similarity. *IEEE Trans. Image Process.* (2004),
690 doi:10.1109/TIP.2003.819861.
691 43. A. Mittal, A. K. Moorthy, A. C. Bovik, No-Reference Image Quality Assessment in the
692 Spatial Domain. *IEEE Trans. Image Process.* **21**, 4695–4708 (2012).
693 44. R. P. J. Nieuwenhuizen, K. A. Lidke, M. Bates, D. L. Puig, D. Grünwald, S. Stallinga, B.
694 Rieger, Measuring image resolution in optical nanoscopy. *Nat. Methods* (2013),
695 doi:10.1038/nmeth.2448.
696 45. A. Amitai, A. Seeber, S. M. Gasser, D. Holcman, Visualization of Chromatin

697 Decompaction and Break Site Extrusion as Predicted by Statistical Polymer Modeling of
698 Single-Locus Trajectories. *Cell Rep.* **18**, 1200–1214 (2017).
699 46. A. Sergé, N. Bertaux, H. Rigneault, D. Marguet, A. Sergé, N. Bertaux, H. Rigneault, D.
700 Marguet, Dynamic multiple-target tracing to probe spatiotemporal cartography of cell
701 membranes. *Nat. Methods*. **5**, 687–694 (2008).
702 47. S. S. P. Rao, M. H. Huntley, N. C. Durand, E. K. Stamenova, I. D. Bochkov, J. T.
703 Robinson, A. L. Sanborn, I. Machol, A. D. Omer, E. S. Lander, E. L. Aiden, A 3D map of
704 the human genome at kilobase resolution reveals principles of chromatin looping. *Cell*.
705 **159**, 1665–1680 (2014).
706 48. S. Beucher, B. Marcotegui, B. P. Marcotegui, "P algorithm, a dramatic enhancement of the
707 waterfall transformation" (2009), (available at http://cmm.ensmp.fr/beucher/publi/).
708 49. W. M. Rand, Objective Criteria for the Evaluation of Clustering Methods. *J. Am. Stat.*
709 *Assoc.* **66**, 846 (1971).
710

711 **Acknowledgments**

712

713 **General**: We acknowledge support from the Pôle Scientifique de Modélisation Numérique, ENS
714 de Lyon for providing computational resources and thank Hazen Babcock and Andrew Seeber
715 (Harvard University) for valuable feedback on the manuscript.

716

717 **Funding:** This work is supported by Agence Nationale de la Recherche (ANR) ANDY and Sinfonie
718 grants.
719

720 **Author contributions:** H.A.S. designed and supervised the project; R.B. designed the data analysis
721 and wrote the code, H.A.S carried out experimental work; R.B. carried out the data analysis; H.A.S.
722 and R. B interpreted results: H.A.S, R.B. and K.B. wrote the manuscript.
723
724 **Competing interests:** The authors declare no competing financial interest.
725
726 **Data and materials availability:** All data needed to evaluate the conclusions in the paper are
727 present in the paper and/or the Supplementary Materials. Additional data related to this paper may
728 be requested from the authors.
729
730 **Figures and Tables**
731 **Figure 1: Temporally resolved super-resolution images of chromatin in U2OS nuclei. A)**
732 Widefield images of U2OS nuclei expressing H2B-PATagRFP are input to a trained convolutional
733 neural network (CNN) and predictions from multiple input frames are summed to construct a super-
734 resolved image of chromatin *in vivo.* **B)** The resolution tradeoff between the prolonged acquisition
735 of emitter localizations (green line) and motion blur due to diffusion of the underlying diffusion
736 processes (purple line). For our experimental data, the localization density per second is $\rho =$
737 $(2.4 \pm 0.1)\ \mu m^{-2} s^{-1}$, the diffusion constant is $D = (3.4 \pm 0.8) \cdot 10^{-3}\ \mu m^2 s^{-1}$ (see
738 Supplementary Figure 8B) and the acquisition time per frame is $\tau = 30\ ms$. The spatial resolution
739 assumes a minimum (69 ± 5 nm) at a time resolution of 360 ms. **C)** Super-resolution images of a
740 single nucleus at time intervals of about 10 seconds. Scale bar is 2 µm. **D)** Magnification of
741 segregated accumulations of H2B within a chromatin-rich region. Scale bar is 200 nm. **E)**
742 Magnification of a stable, but dynamic structure (arrows) over three consecutive images. Scale bar
743 is 500 nm. **F)** Fourier Ring Correlation (FRC) for super-resolved images resulting in a spatial
744 resolution of 63 ± 2 nm.

745

746 **Figure 2: Chromatin blob identification and characterization of imaged and modeled**
747 **chromatin. A)** Super-resolved images show blobs of chromatin (left). These blobs are segmented
748 (Materials and Methods, Supplementary Note 1) and individually labeled by random color (right).
749 Magnifications of the boxed regions are shown. Scale bars: whole nucleus 2 μm, magnifications
750 200 nm. **B)** Generation of super-resolution images and blob identification and characterization for
751 a 25 Mbp segment of chromosome 1 from GM12878 cells as simulated in Qi *et al.* (*24*). Beads (5
752 kb genomic length) of a simulated polymer configuration within a 200 nm thick slab are projected
753 to the imaging plane, resembling experimental super-resolved images of live chromatin. Blobs are
754 identified as on experimental data. **C)** From the centroid positions, the nearest-neighbor distance
755 (NND) distributions are computed for up to 40 nearest neighbors (blue to red). The envelope of the
756 k-NND distributions (black line) shows peaks at approximately 95 nm, 235 nm, 335 nm and 450
757 nm (red dots). **D)** k-NND distributions as in B) for simulated data. **E)** Area distribution of
758 experimental and simulated blobs. The distribution is in both cases well described by a lognormal
759 distribution with parameters $(\mathbf{3.3} \pm \mathbf{2.8}) \cdot \mathbf{10^{-3}}$ μm^2 for experimental blobs and $(\mathbf{3.1} \pm \mathbf{3.2}) \cdot$
760 $\mathbf{10^{-3}}$ μm^2 for simulated blobs (mean $\pm$ standard deviation). **F)** Eccentricity distribution for
761 experimental and simulated chromatin blobs. Selected eccentricity values are illustrated by ellipses
762 with the corresponding eccentricity. Eccentricity values range from 0, describing a circle, to 1,
763 describing a line. Prominent peaks arise due to the discretization of chromatin blobs in pixels.

764 **Figure 3: Chromatin blobs on modeled chromosomes consist of continuous loci along the**
765 **genome and exhibit a TAD-like time-averaged conformation. A)** Gap length between beads
766 belonging to the same blob. An exemplary blob with small gap length is shown. The blob is mostly
767 made of consecutive beads being in close spatial proximity. **B)** A representative polymer
768 configuration is colored according to chromatin states (red: active, green: inactive, blue:
769 repressive). **C)** The cumulative distribution function of clusters within active, inactive and

770 repressive chromatin. Inset: Mean area of clusters within the three types of chromatin. The
771 distributions are all significantly different from each other as determined by a two-sample
772 Kolmogorov-Smirnov test ($p < 10^{-50}$). **D)** Distribution of the continuous residence time of any
773 monomer within a cluster (0.5 $\pm$ 0.3 s; mean $\pm$ standard deviation). Inset: Continuous residence
774 time of any monomer within a slab of 200 nm thickness (1.5 $\pm$ 1.6 s; mean $\pm$ standard deviation).
775 **E)** The blob association strength between any two beads is measured as the frequency at which any
776 two beads are found in one blob. The association map is averaged over all simulated configurations
777 (upper triangular matrix; from simulations) and experimental Hi-C counts are shown for the same
778 chromosome segment (lower triangular matrix; from Rao *et al.* (*47*)). The association and Hi-C
779 maps are strongly correlated (Pearson's correlation coefficient PCC = 0.76) **F)** Close-up views
780 around the diagonal of Hi-C-like matrices. The association strength is shown together with the
781 inverse distance between beads (upper panel; PCC = 0.85) and with experimental Hi-C counts
782 (lower panel; as in E)).

783

784 **Figure 4: Super-resolution chromatin dynamics. A)** A time series of super-resolution images
785 (left panel) is subject to Optical Flow (right panel). **B)** (i-ii) Two subsequent images of chromatin.
786 Magnifications show prominent mobile blobs on the nuclear periphery in both images (colored
787 arrows). (iii) The flow field and corresponding magnification are shown on top of a fused image of
788 both super-resolved images in (i) and (ii) (green and purple respectively, co-localization are white).
789 The flow field is colored according to the direction of vectors (see color wheel) **C)** As for B) in the
790 nuclear interior. Scale bars: whole nucleus 2 µm, magnifications 500 nm. Flow vectors are not
791 drawn to scale and down-sampled 8-fold for clarity. **D)** Blobs of a representative nucleus (see
792 Supplementary Movie 1) are labeled by their NND (left), area (middle) and flow magnitude (right).
793 Colors denote the corresponding parameter magnitude.

794

Figure 5: Spatio-temporal correlations between structural and dynamic parameters. A) The spatial auto- and cross-correlation between parameters were computed for different time lags. The graphs depict the correlation over space lag for each parameter pair and different colors denote the time lag (increasing from blue to red). **B)** Illustration of the instantaneous relationship between local chromatin density and dynamics. The blob density is shown in blue; the magnitude of chromatin dynamics is shown by red arrows. The consistent negative correlation between NND and flow magnitude is expressed by increased dynamics in regions of high local blob density.

Figure 6: Chromatin feature extraction. A) The six-dimensional parameter space is input to the t-SNE algorithm and projected to two dimensions. **B)** The 2D embedding of an exemplary data set is shown and colored according to the magnitude of each input feature (blue to red, the parameter average is shown in beige) **C)** Points below the first (blue) and above the third (red) quartile points of the corresponding parameter are marked and the parameters are ranked according to the fraction of nearest neighbors which fall in one of the marked regions. **D)** Data points marked below the first or above the third quartile points are labeled according to the feature in which they were marked. Priority is given to the feature with the higher nearest-neighbor fraction if necessary. **E)** t-SNE analysis is carried out for each nucleus over the whole time series and it is counted how often a parameter ranked 1st. The results are visualized as a pie chart. The NND predominantly ranks 1st in about 2/3 of all cases. **F)** Marked points in C-D) are mapped back onto the corresponding nuclei and the cumulative distribution function (CDF) over space is shown.

Figure 1

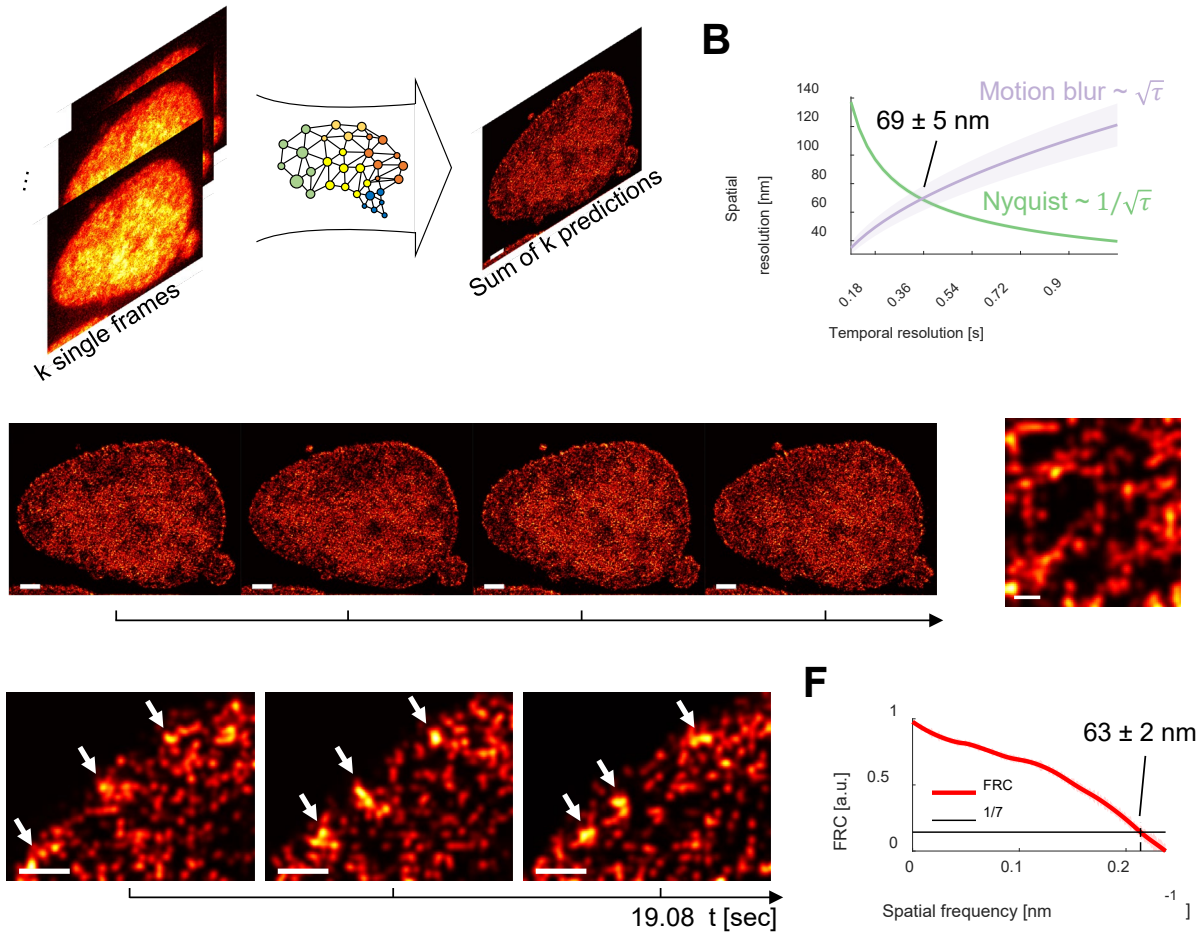
k single frames
Sum of k predictions
B
Motion blur ~ $\sqrt{\tau}$
69 ± 5 nm
Nyquist ~ $1/\sqrt{\tau}$
Spatial resolution [nm]
140
120
100
80
60
40
0.18
0.36
0.54
0.72
0.9
Temporal resolution [s]
F
63 ± 2 nm
FRC
1/7
FRC [a.u.]
1
0.5
0
0
0.1
0.2
Spatial frequency [nm^{-1}]
19.08 t [sec]

Figure 2

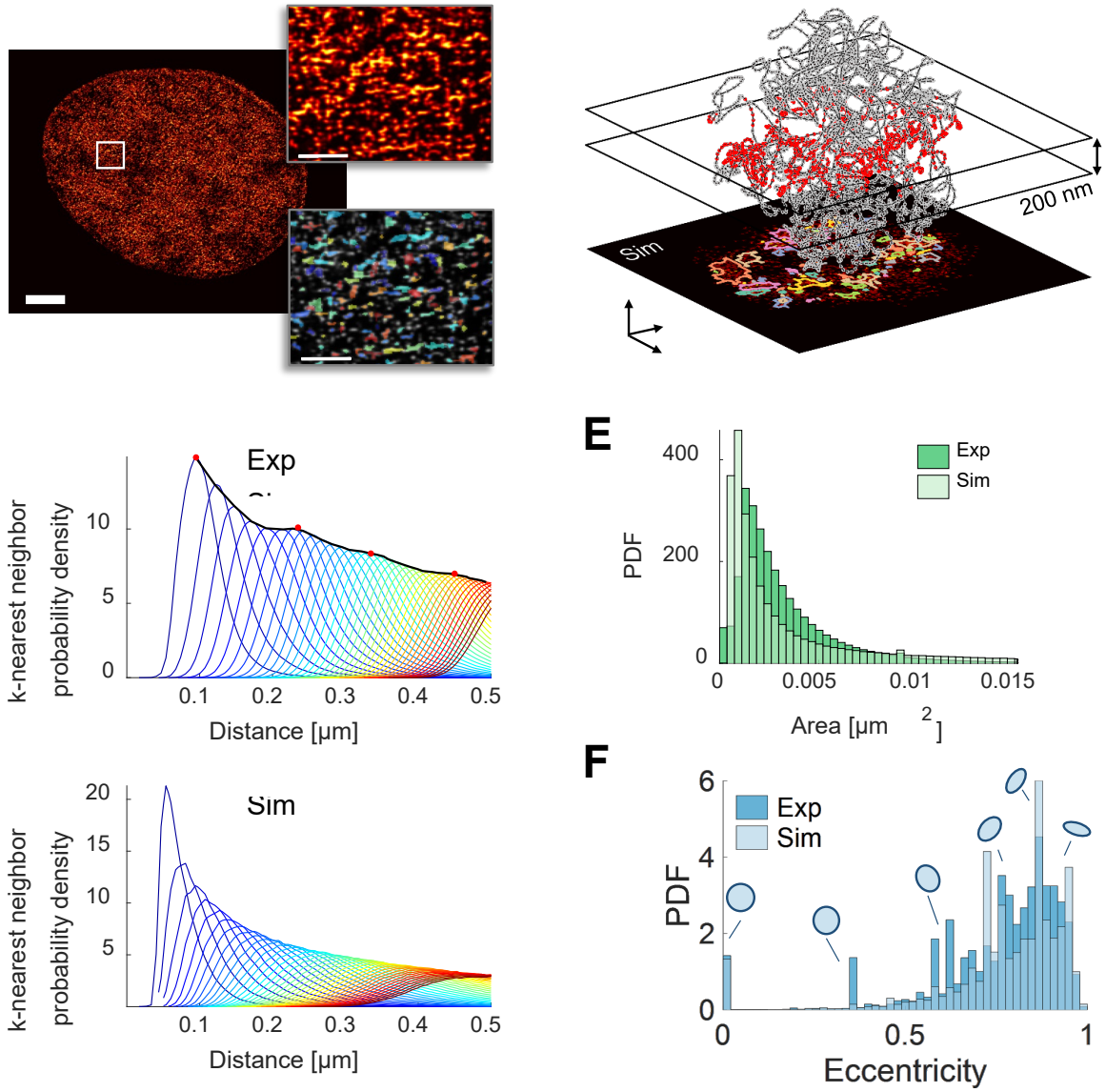
200 nm
Sim
Exp
k-nearest neighbor probability density
Distance [μm]
Sim
E
Exp
Sim
PDF
Area [μm 2]
F
Exp
Sim
PDF
Eccentricity

834 **Figure 3**

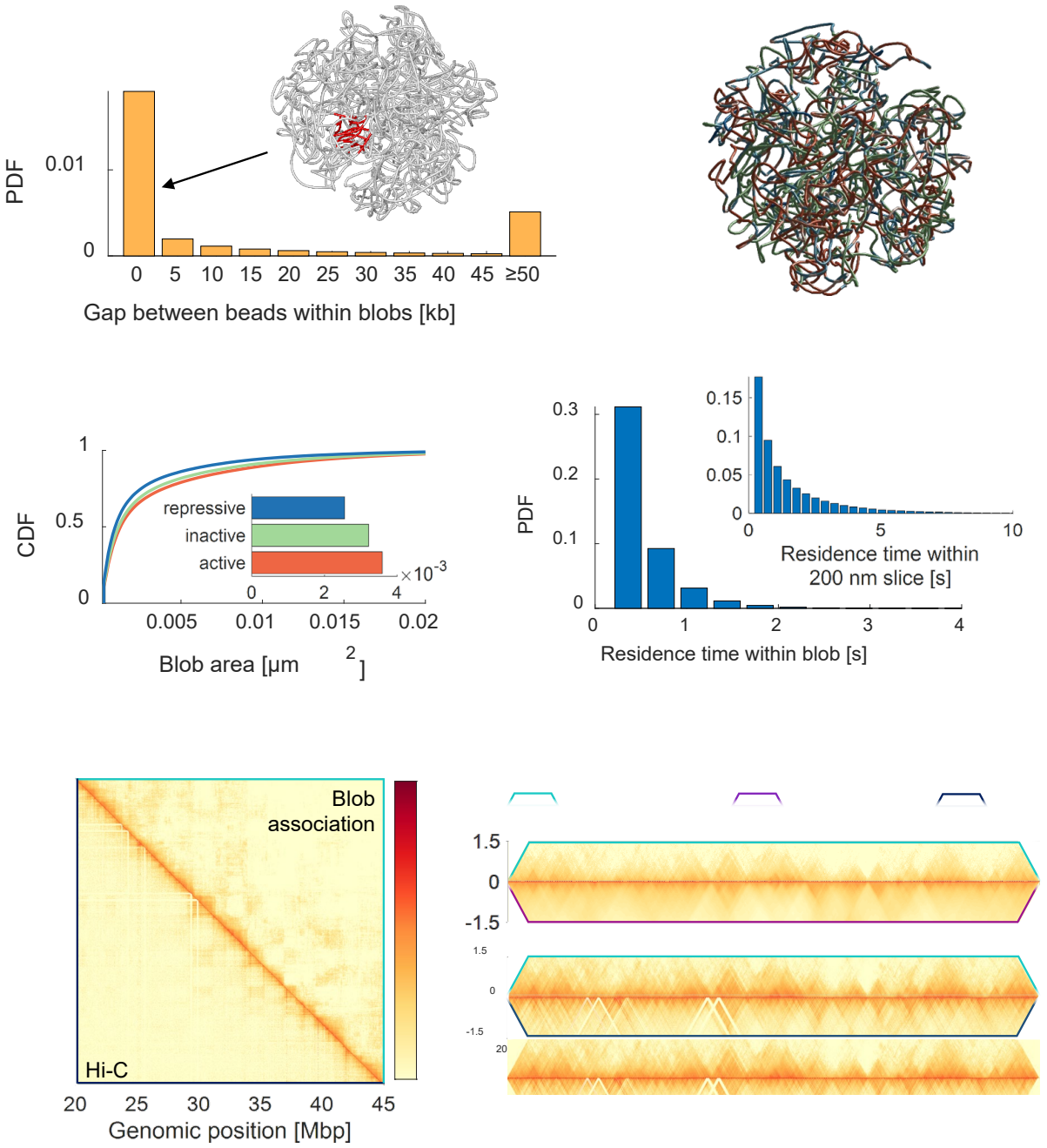

835

836

837

838

839

840 **Figure 4**

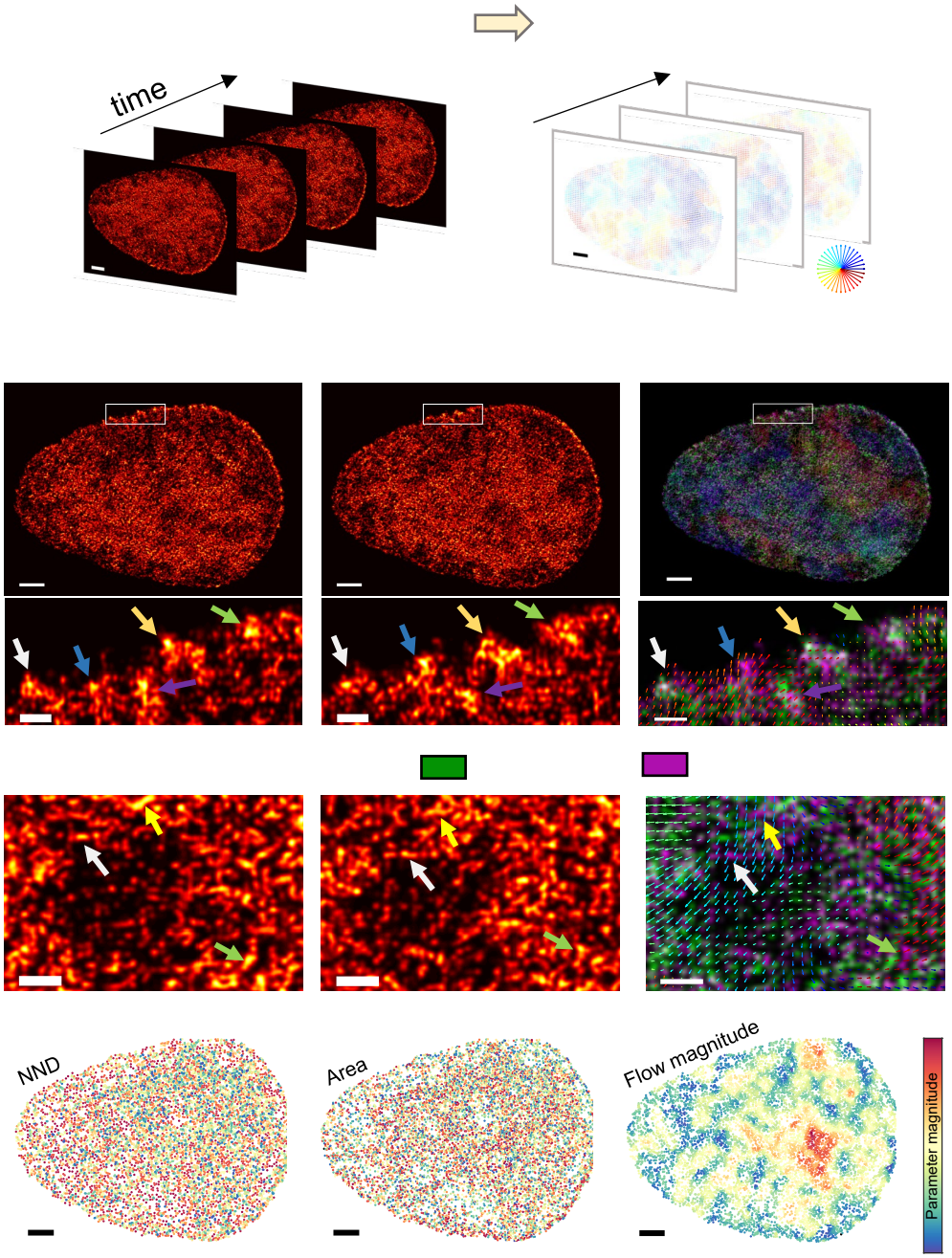

841

842

843

844

845 **Figure 5**

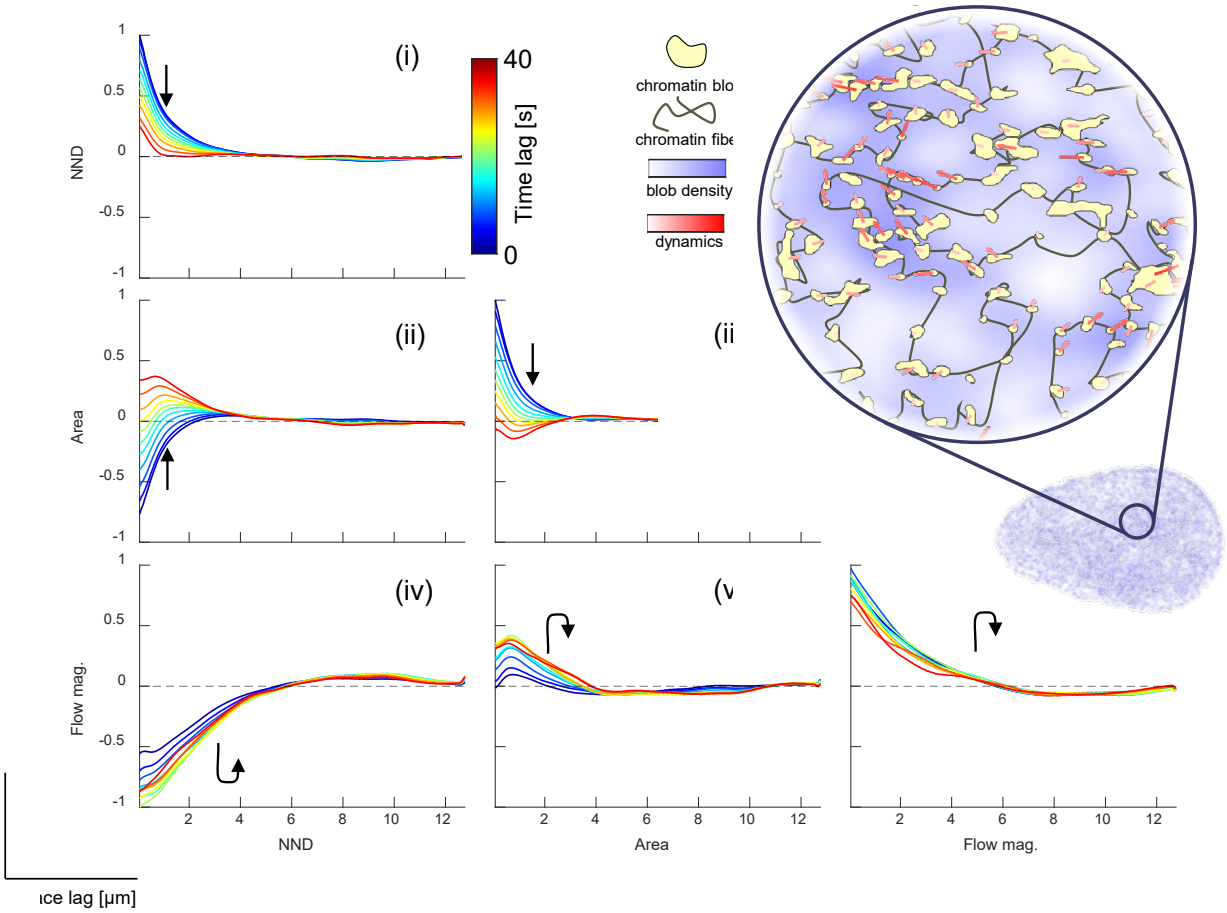

846

847

848

849

850

851

852

853

854

855 **Figure 6**

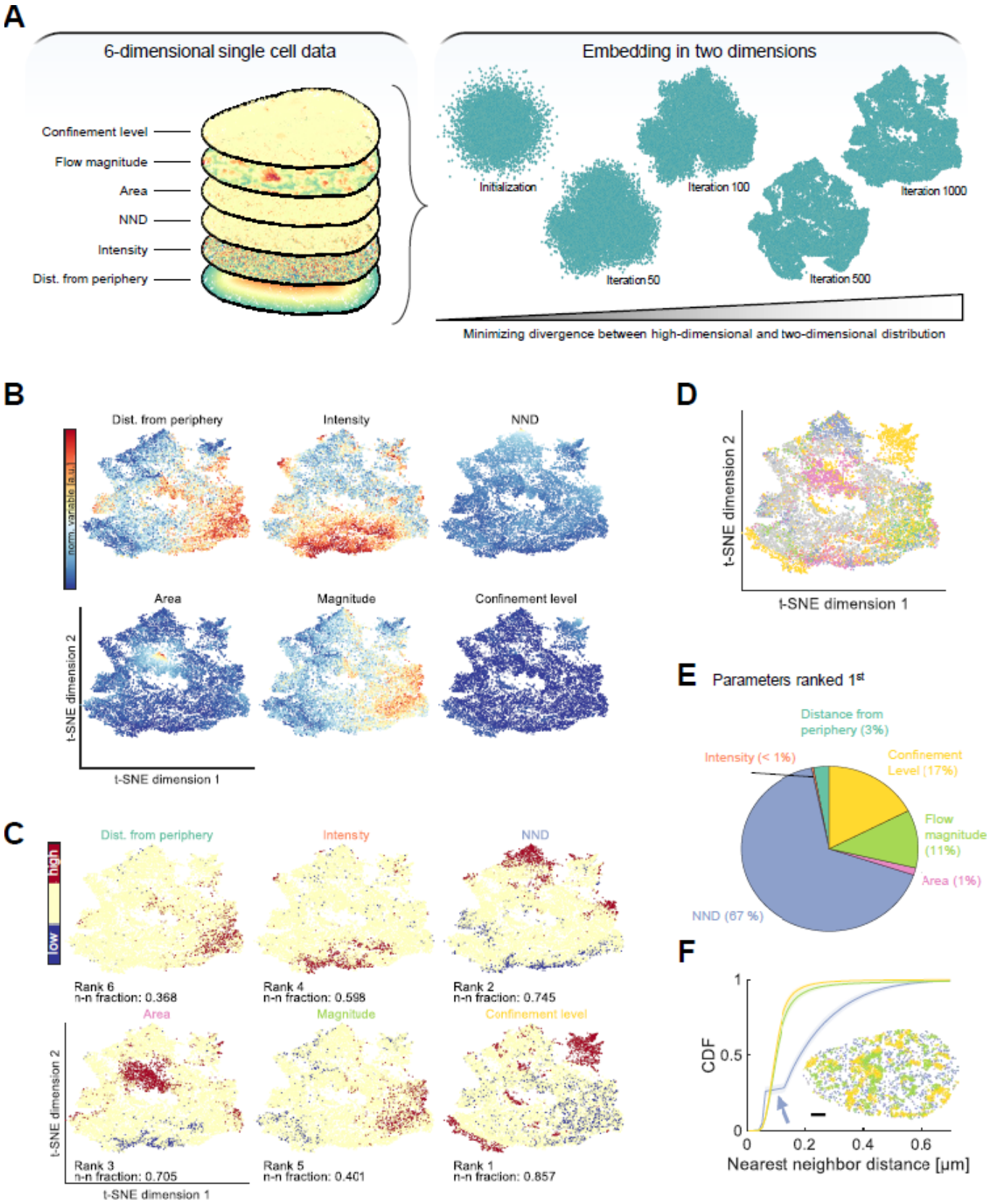

856

857

858

SUPPLEMENTARY MATERIAL

Coupling chromatin structure and dynamics by live super-resolution imaging

R. Barth[1, 2,] K. Bystricky[1] and H. A. Shaban[,1, 3, †, *]

1: Laboratoire de Biologie Moléculaire Eucaryote (LBME), Centre de Biologie Intégrative (CBI), CNRS; University of Toulouse, UPS; 31062 Toulouse; France

2: Department of Bionanoscience, Delft University of Technology, 2628 CJ Delft, The Netherlands

3: Spectroscopy Department, Physics Division, National Research Centre, Dokki, 12622 Cairo, Egypt

†: Present address: Center for Advanced Imaging, Northwest Building, Harvard University, Cambridge, MA, 02138, USA

*: To whom correspondence may be addressed: Haitham A. Shaban. Email hshaban@fas.harvard.edu

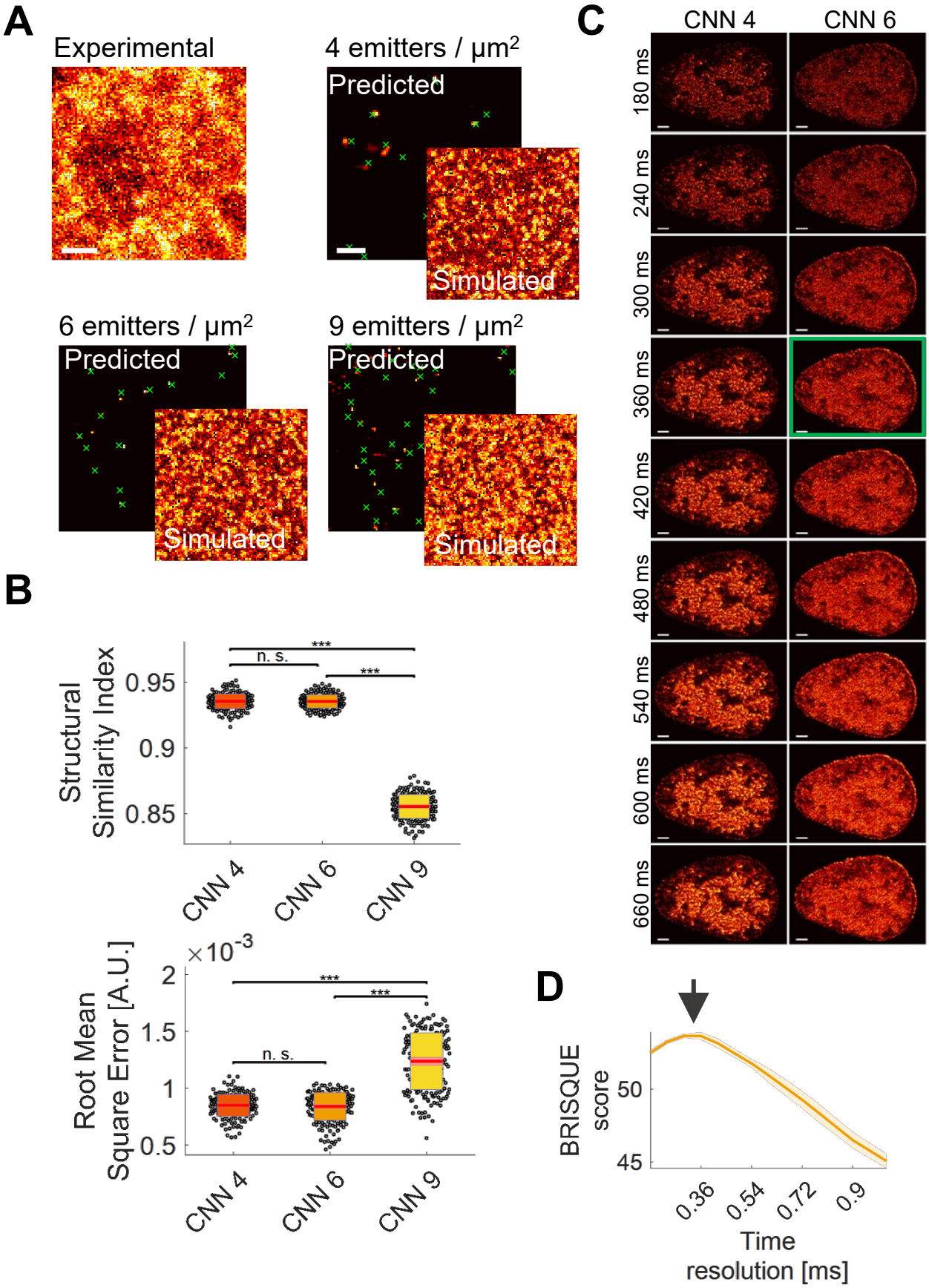
A
Experimental
4 emitters / μm²
Predicted
Simulated
6 emitters / μm²
Predicted
Simulated
9 emitters / μm²
Predicted
Simulated
B
Structural Similarity Index
0.95
0.9
0.85
n. s.
***
***
CNN 4
CNN 6
CNN 9
Root Mean Square Error [A.U.]
×10⁻³
2
1.5
1
0.5
n. s.
***
***
CNN 4
CNN 6
CNN 9
C
CNN 4
CNN 6
180 ms
240 ms
300 ms
360 ms
420 ms
480 ms
540 ms
600 ms
660 ms
D
BRISQUE score
50
45
0.36
0.54
0.72
0.9
Time resolution [ms]

873

Supplementary Figure 1: CNN training and time-resolution determination. A) Experimental and simulated widefield images with varying labeling density. Predictions by the trained CNNs are shown as false-color images and the ground truth emitter positions are overlaid as green crosses. Scale bar for experimental widefield image is 2 µm, simulated images are the same size. Scale bar on predictions are 200 nm. **B)** The accuracy of the trained CNNs was evaluated using the Structural Similarity Index and the Root Mean Square Error (Materials and Methods). The CNN trained with 9 emitters per μm^2 (CNN 9) performs significantly worse than the other two CNNs. Statistical significance assessed by a two-sample t-test (*** $p < 0.001$). **C)** Predictions from single acquired images are summed over different times from 360 ms to 1020 ms. A subset of reconstructions up to a time resolution of 660 ms are shown for CNN 4 and CNN 6. Scale bar is 2 µm. **D)** The structural image quality as quantified by BRISQUE (*43*) for CNN 6 at varying temporal resolution. The optimal (maximum) value is found at a time resolution of 360 ms.

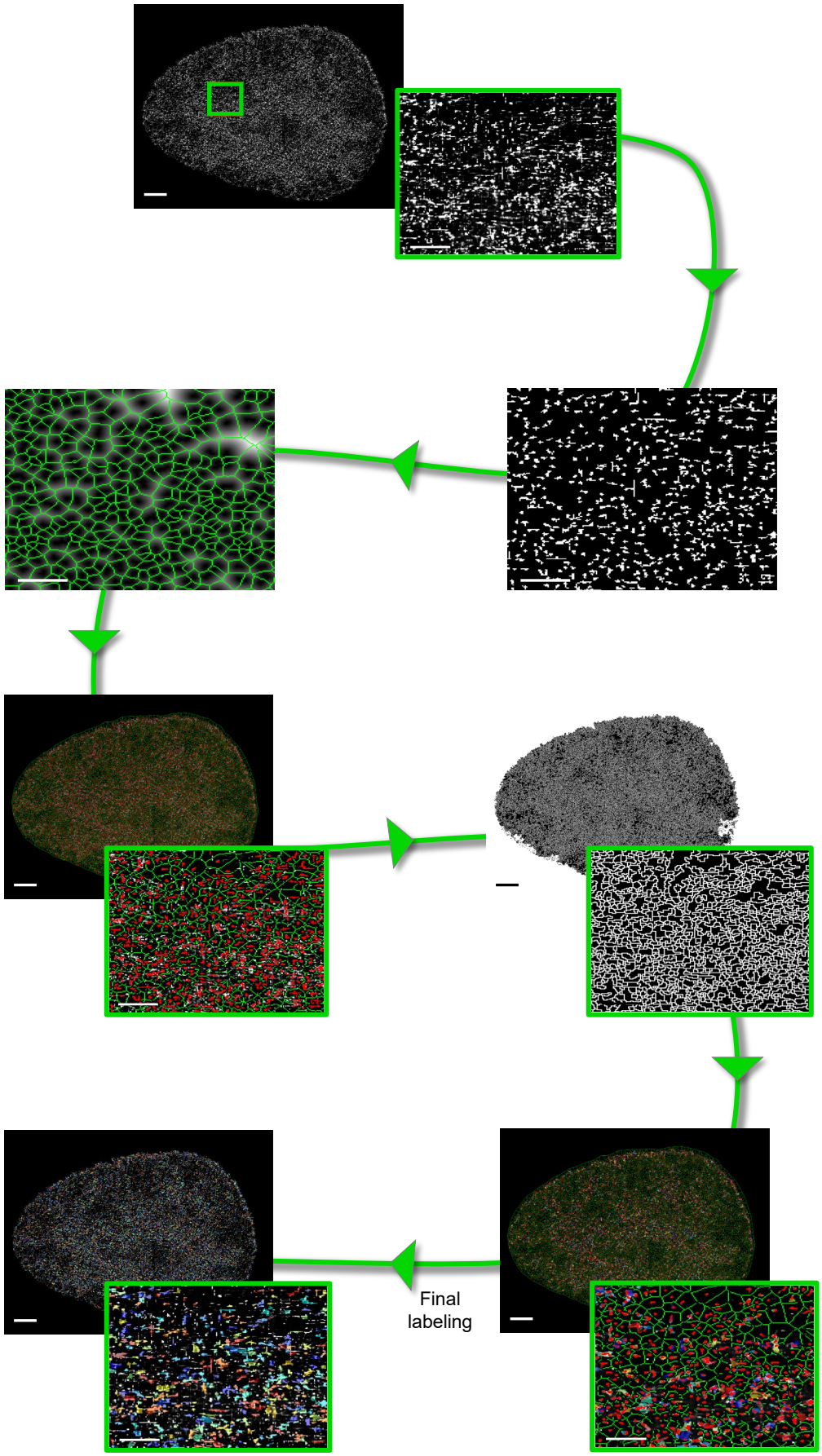

887

Supplementary Figure 2: Chromatin blob identification pipeline. A) A grayscale image as output from the Deep-PALM algorithm is to be segmented. Magnified views correspond to the red rectangle. **B)** Foreground pixels are marked by finding the regional maxima. Additionally, very bright pixels (i.e. those with $\boldsymbol{I} > \mathbf{0.99} \cdot \boldsymbol{I_{max}}$) are marked as foreground. Only the magnification is shown. **C)** The watershed algorithm (without markers) is applied to the distance transform of the foreground mask. The resulting watershed lines represent lines in between pixels marked as foreground and therefore represent pixels of (local) low intensity, i.e. background markers. The background mask is corrected for pixels which nevertheless exert high intensity (i.e. those with $\boldsymbol{I} > \mathbf{0.8} \cdot \boldsymbol{I_{max}}$). Only the magnification is shown. **D)** Input image with the foreground (red) and background (green) markers superimposed. **E)** The watershed algorithm is applied to the gradient of the input image with minima imposed on pixels belonging to fore- or background. **F)** The regions defined by watershed lines (the basins) are post-processed in order to keep only those whose mean and median intensity exceed a threshold of $\mathbf{0.1} \cdot \boldsymbol{I_{max}}$. **G)** Resulting segmentation of the input image. Scale bars correspond to 2 µm and 0.5 µm in the full and magnified regions respectively.

SUPPLEMENTARY NOTE 1

Segmentation performance

The marker-assisted watershed segmentation pipeline developed to segment chromatin blobs in super-resolved images is tested against other state-of-the-art segmentation algorithms in order to validate its performance. We evaluated our approach against three fully automated improvements of the widely spread watershed algorithm: the enhanced waterfall algorithm, the 'standard' algorithm, and the P-algorithm (*48*). To this end, we simulated images which closely resemble experimental super-resolved images of histone-labeled chromatin. We generated random shapes by thresholding randomly generated 1/f noise and gave intensity to the shapes according to experimental images. An exemplary simulated and experimental image is shown in Supplementary Figure 3A, B. The segmentation result of an exemplary simulated image is shown in Supplementary Figure 3D, I. We used the Rand index as a measure of the similarity of two segmentation algorithms. In particular, the Rand index is computed between the ground truth and the segmentation result of each algorithm as an estimate of the likelihood of a correctly classified element. An image segmentation problem can be formulated as a partitioning of the image pixels into several subsets. Let P denote the set of n pixels to be segmented, $G = \{G_1, \dots, G_g\}$ denotes the ground truth segmentation of n pixels into g subsets and $R = \{R_1, \dots, R_r\}$ denotes the resulting segmentation into r subsets from an algorithm to test. The number of agreements between G and R consists of (i) the true positives (TP), i.e. the pairs of elements in P that are in the same subset in G and R and (ii) the true negatives (TN), i.e. the pairs of elements in P that are not in the same subset in G and not in R. Likewise, the number of disagreements consists of (iii) the false negatives (FN), i.e. elements in P that are in the same subset in G but not in R and (iv) the false positives (FP), i.e. elements in P that are not in the same subset in G but that are in R. Taken together, the Rand index expresses the number of agreements over the total number of pairs, i.e. agreements and disagreements (*49*):

$$\text{Rand Index} = \frac{TP + TN}{TP + TN + FN + FP} = \frac{TP + TN}{\binom{n}{2}} \tag{6}$$

The Rand index ranges from 0 to 1 and gives the fraction of matching pairs of pixels in the ground truth and computed segmentation. Our custom marker-controlled watershed algorithm performs significantly better than other tested algorithms, with a Rand index of about 75%.

To further validate the segmentation algorithm, the blob segmentation on experimental images of chromatin (Supplementary Figure 4A) was compared to images, in which emitters were randomly distributed (Supplementary Figure 4B). On random images, the blob density was ~ 19-fold reduced compared to segmentation on experimental images (Supplementary Figure 4C) and the blob area was about one order of magnitude smaller (Supplementary Figure 4D). These results show that blobs were identified due to the appearance of chromatin as blobs and not due to apparent grouping of randomly distributed emitters.

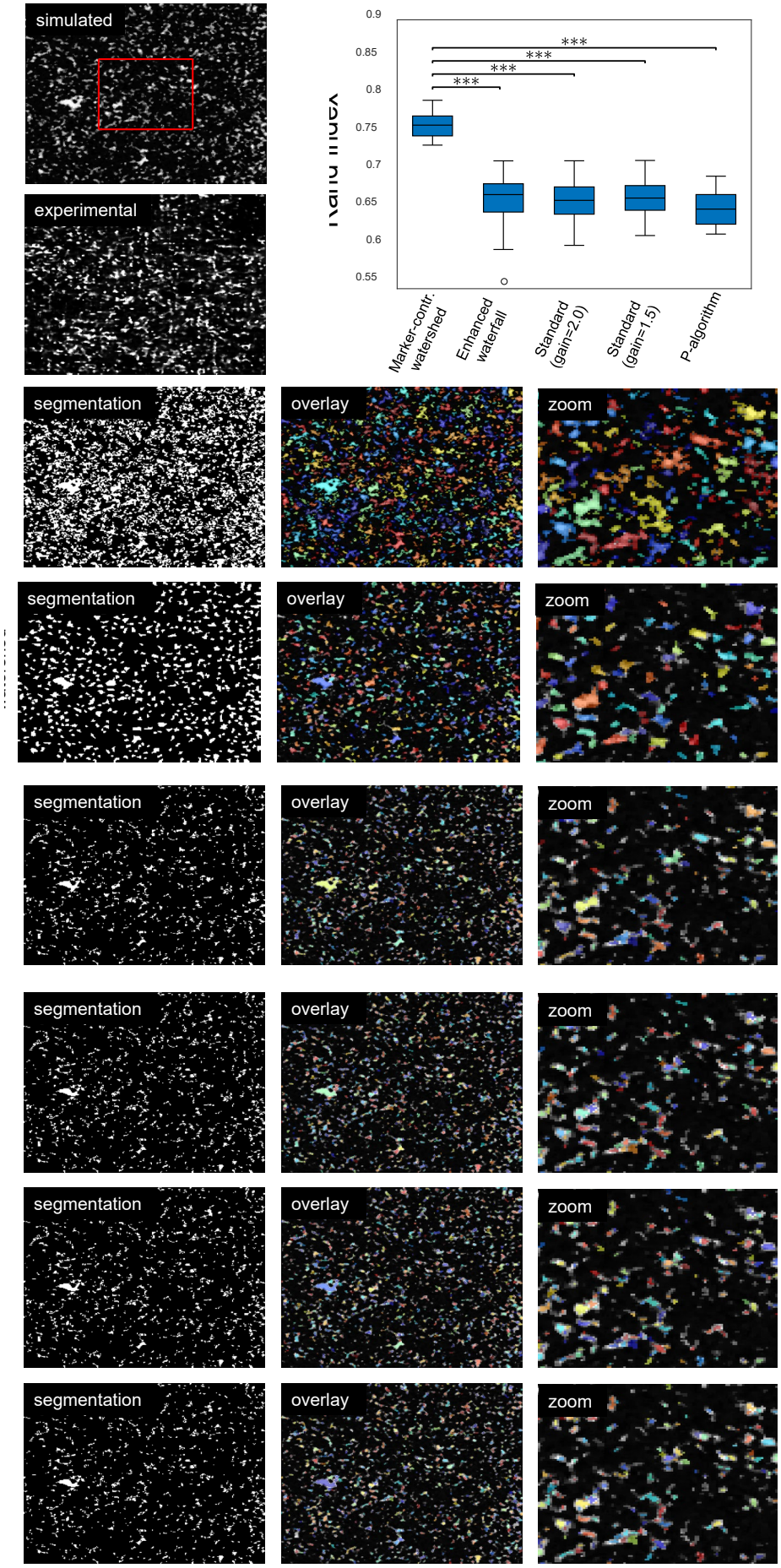
simulated
experimental
0.9
0.85
0.8
0.75
0.7
0.65
0.6
0.55
***
***
***
***
Marker-contr. watershed
Enhanced waterfall
Standard (gain=2.0)
Standard (gain=1.5)
P-algorithm
segmentation
overlay
zoom
segmentation
overlay
zoom
segmentation
overlay
zoom
segmentation
overlay
zoom
segmentation
overlay
zoom
segmentation
overlay
zoom

Supplementary Figure 3: Performance of segmentation algorithms on super-resolved images of chromatin *in vivo*. A) Exemplary simulated image for which the ground truth segmentation is known, used to compare different segmentation algorithms. The section in the red triangle is magnified in D-I). **B)** Exemplary experimental image to be compared to the simulated image. **C)** The Rand index reveals that our custom maker-controlled watershed algorithm significantly outperforms all other tested algorithms. Statistical significance assessed from 20 independent segmentation runs by a two-sample t-test (*** $p < 0.001$). **D)** Binary image (right) displaying the ground truth segmentation of the simulated image. Different segments are randomly colored for clarity and the magnified region marked in A) is shown. **E-I)** Exemplary segmentation results from the tested algorithms.

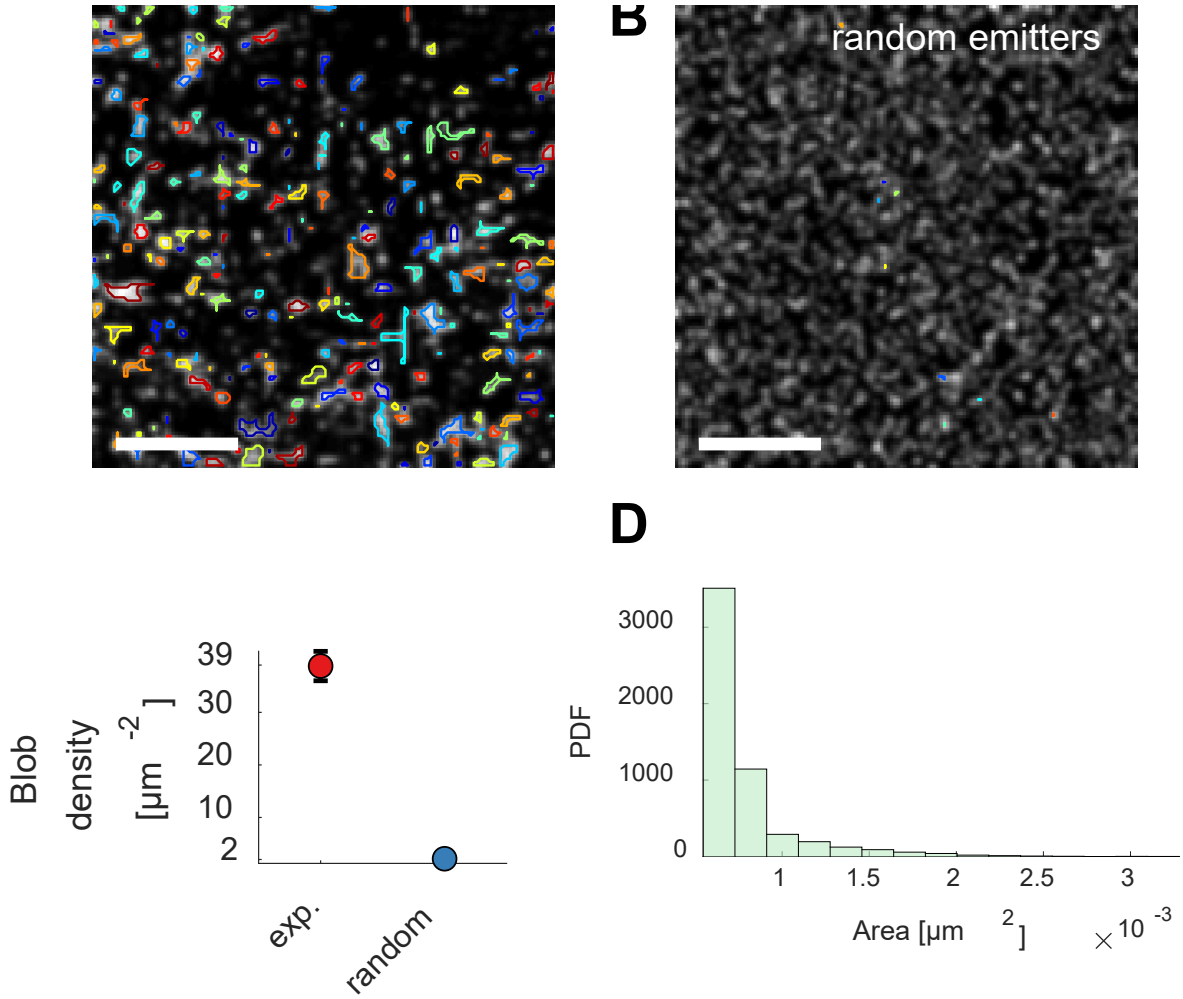

Supplementary Figure 4: Segmentation on images of randomly distributed emitters. A) An exemplary super-resolved image of chromatin *in vivo*, the identified blobs are overlaid and randomly colored. **B)** Emitters were randomly distributed, and the segmentation algorithm was applied to those images. The number of emitter was matched to the number of beads of the modeled chromosomes within the imaging volume (compare Figure 2B). Scale bar is 0.5 µm. **C)** The blob density for blobs identified on experimental images and images containing randomly distributed emitters. Experimental images contained ~20-fold more blobs than could be identified using random images. **D)** Area distribution for blobs identified on images containing randomly distributed emitters (mean ± std.: $(\mathbf{0.4 \pm 0.2}) \cdot \mathbf{10^{-3}}$ µm^2).

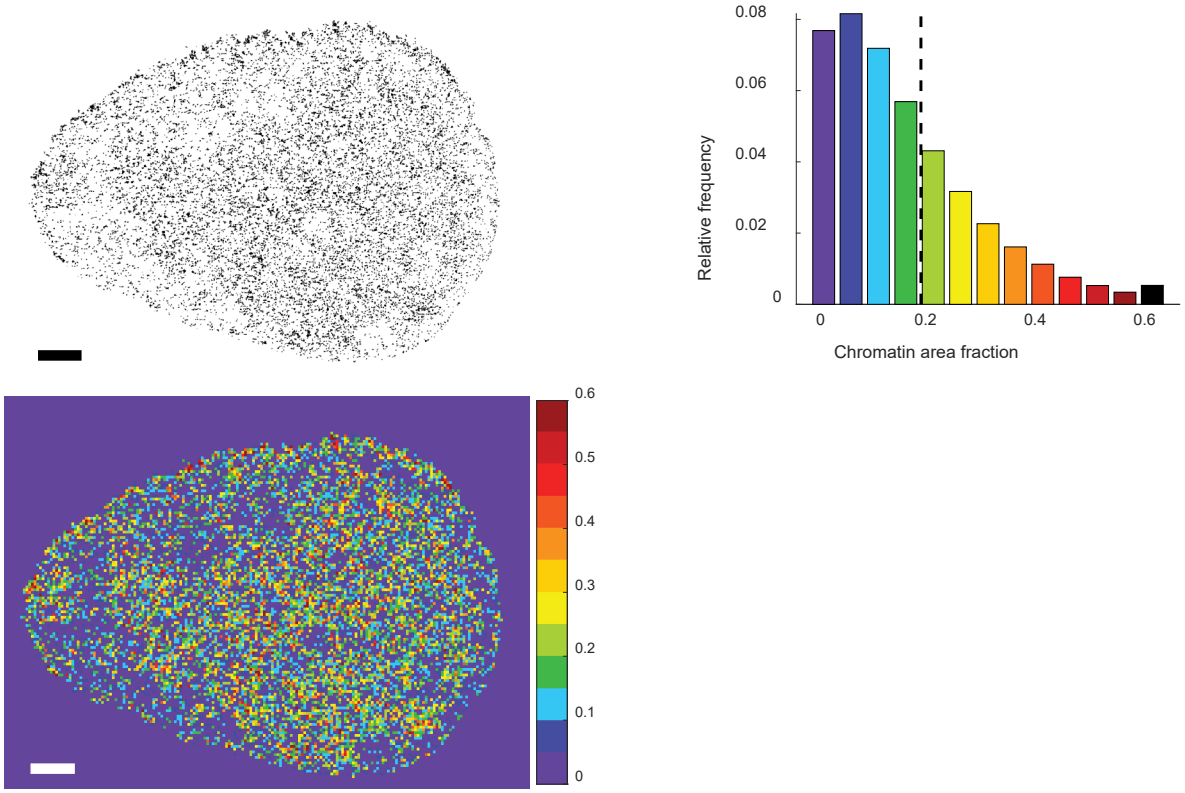

Supplementary Figure 5: Chromatin area fraction. A) Segmented images are divided into boxes with dimensions 120 nm x 120 nm and the chromatin area fraction is computed for each box. Exemplary, a map of chromatin area fractions is shown color-coded from low to high chromatin density (purple to red). Scale bar is 2 µm. **B)** Histogram of the observed chromatin area fractions. The black line denotes 18 ± 14 % (mean ± std).

SUPPLEMENTARY NOTE 2

Suitability of Optical Flow for super-resolution images of chromatin

Optical Flow is used to compute a flow field between two subsequent images in scenarios in which dynamic information cannot be retrieved from single-particle tracking approaches, for example, due to high labeling densities (*19*). Optical Flow algorithms are generally evaluated with respect to the angular error (AE), a measure for the error in the direction between a computed and a ground truth vector. Likewise, the endpoint error (EE) is a measure for the error in the magnitude. For two computed vectors $\boldsymbol{a}$ and $\boldsymbol{b}$, the AE and EE are computed as (*26*)

$$AE = \cos^{-1}\left(\frac{\boldsymbol{ab}}{|\mathbf{a}||\mathbf{b}|}\right) \tag{7}$$

and

$$EE = |\mathbf{a} - \mathbf{b}| \tag{8}$$

Current Optical Flow algorithms achieve sub-pixel EE and AE of around 20° for bulk chromatin imaging. Here, we prove that the Optical Flow algorithm used previously for conventional microscopes (*19*, *26*) results in comparable AE and EE values using super-resolved time series of chromatin. To this end, ground truth data is simulated as described previously (*19*). A density of 6 emitters per μm^2 and an acquisition time of 30 ms was used to resemble experimental data (Supplementary Figure 1). The images were either summed up directly in sets of 12 in order to achieve experimental time resolution of 360 ms or first processed by Deep-PALM and then summed. Optical Flow was computed for both sets and the AE and EE were computed. Exemplary simulated images and ground truth vectors, as well as computed flow fields, are superimposed in Supplementary Figure 6A-B. The resulting AE and EE from 20 independent runs are summarized in Supplementary Figure 6C. Optical Flow on super-resolved images did not significantly change the accuracy in direction, however the endpoint error is slightly smaller for flow fields computed on super-resolved images. These results thus validate Optical Flow for the use on super-resolution time series of chromatin.

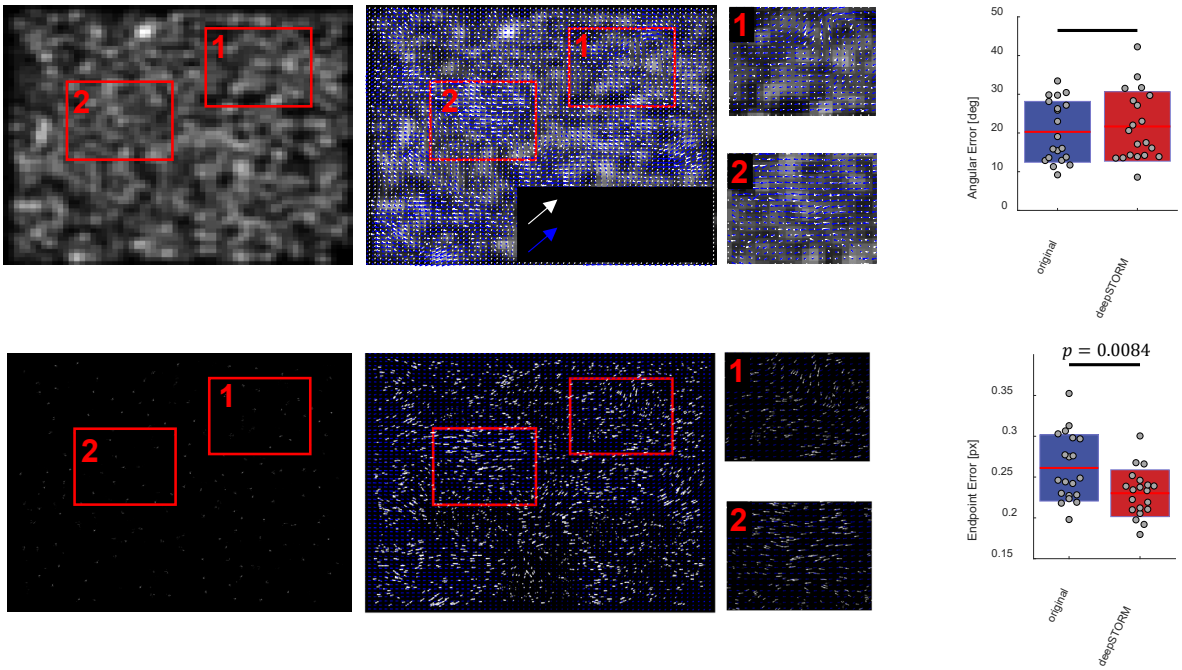

Supplementary Figure 6: Performance of Optical Flow on conventional and super-resolved images. A) Exemplary simulated conventional fluorescence microscopy images (left), ground truth and estimated flow field (middle). Magnified regions as indicated by the red boxes (right). **B)** As

A) for images analyzed with Deep-PALM. For visualization, only every eighth vector is shown (Deep-PALM images are up-sampled 8-fold compared to the input images). **C)** Angular and endpoint error over 20 independent sets of simulated images. Statistical significance was determined by a two-sided t-test.

Supplementary Movie 1: Time series of super-resolved chromatin structure and dynamics. The centroid positions of each identified blob are mapped onto the nucleus and colored according to their nearest-neighbor distance, area, mean displacement direction, and magnitude. Colors are given such that the respective maximum parameter value over the whole image series is red, the minimum parameter value is blue. Colors thus indicate parameter values relative to the parameter range. Displacement direction is color-coded according to the color-wheel shown.

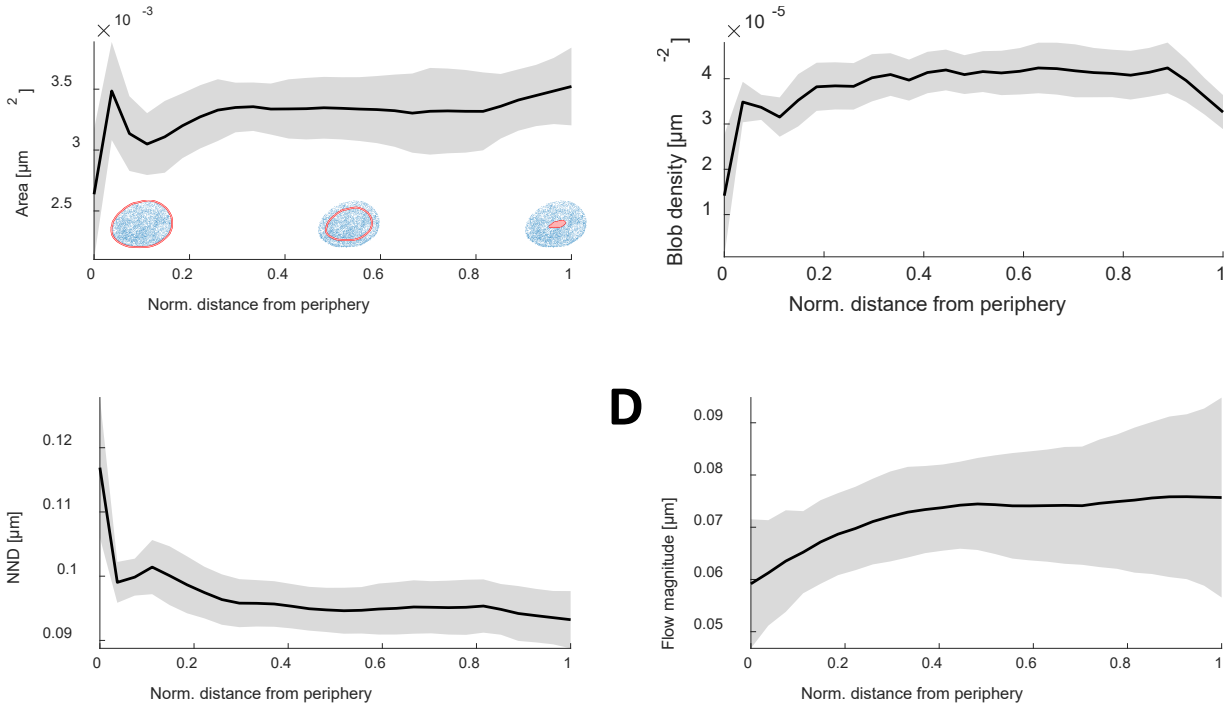

Supplementary Figure 7: Structural and dynamic parameters are dependent on the proximity to the nuclear periphery. A) The average area, **B)** NND, **C)** density and **D)** flow magnitude versus the normalized distance from the nuclear periphery (0 is on the periphery and 1 is at the center of the nucleus). Line and shaded area denote the mean $\pm$ standard error.

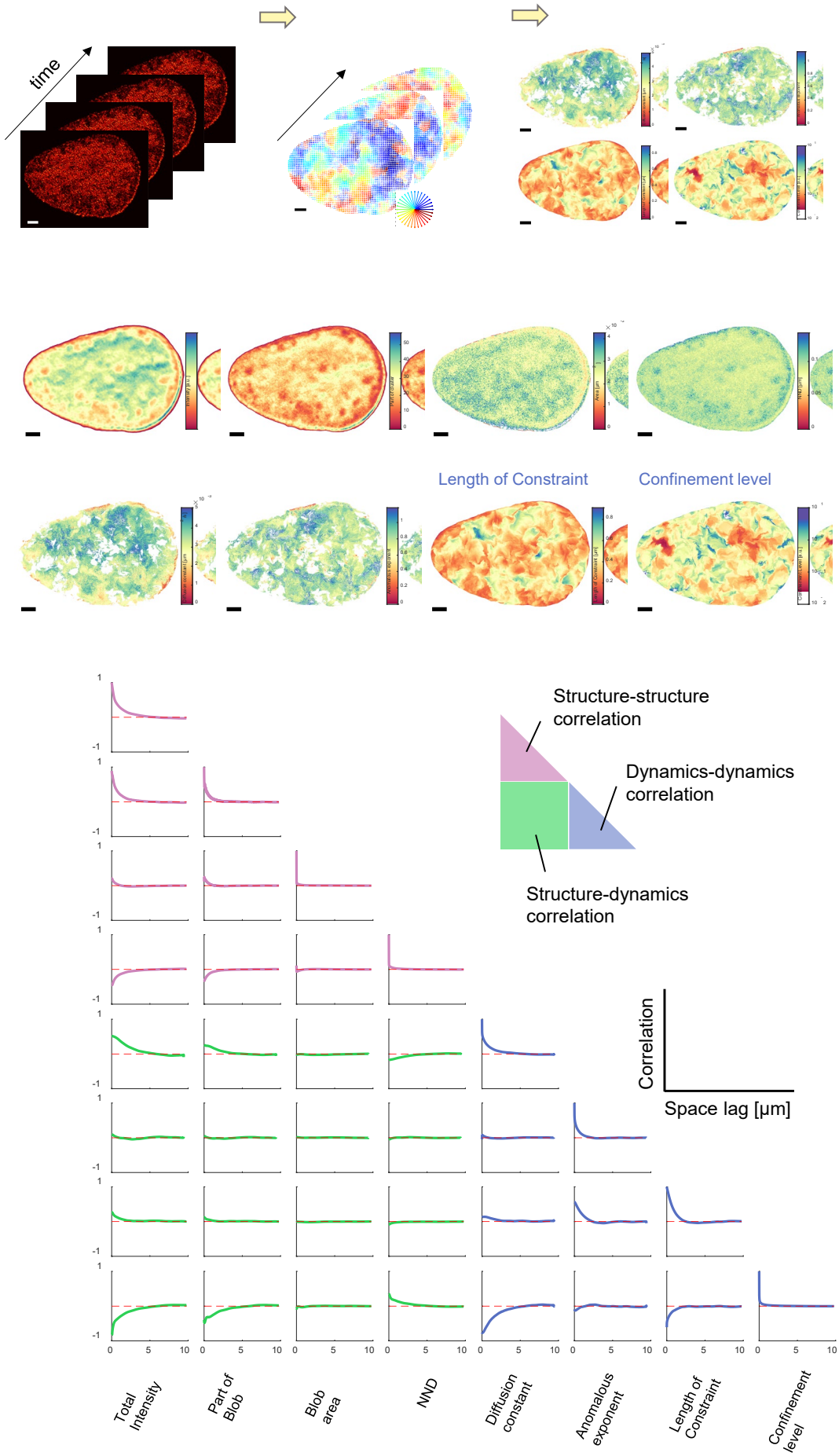
time
Length of Constraint
Confinement level
Structure-structure correlation
Dynamics-dynamics correlation
Structure-dynamics correlation
Correlation
Space lag [μm]
Total Intensity
Part of Blob
Blob area
NND
Diffusion constant
Anomalous exponent
Length of Constraint
Confinement level

1018 **Supplementary Figure 8: Global spatial correlation of structural and dynamic parameters.**
1019 **A)** Illustration of the Hi-D workflow. A time series of super-resolution images (left panel) is input
1020 to the Optical Flow algorithm resulting in flow fields with a pixel size of 13.5 nm (middle panel).
1021 By trajectory reconstruction and motion classification, quantities describing the underlying bulk
1022 motion are computed. **B)** Eight parameters characterizing the global chromatin structure and
1023 dynamics during the whole time series are shown. The structural parameters (upper row) are the
1024 total intensity of super-resolved images, the counts how often each pixel was identified as part of a
1025 chromatin blob, the average blob area per pixel and the average nearest-neighbor distance for each
1026 pixel. Dynamic parameters are the diffusion constant and anomalous exponent, which was
1027 computed by regression of mean squared displacement curves (Materials and Methods), the length
1028 of constraint and the average confinement level. Scale bar is 3 µm. **C)** The spatial correlation
1029 between all combinations of structural and dynamic parameters over space lag is shown.

1030

1031

SUPPLEMENTARY NOTE 3

t-SNE and its robustness with respect to distance metrics and perplexity

High-Dimensional parameter space is input to the t-SNE algorithm. The underlying principle is that data points, which are similar with respect to a number of factors (dimensions) lie close in high-dimensional space (employing a certain distance metric). The mapping into lower dimensionality (for instance in 2D) by t-SNE is initialized by assigning each point a random position in 2D (Figure 6A). Illustratively, a set of springs between all data points exert a repelling or attractive force on each other depending on if the current distances between data points in 2D represent the distances between the data points in high-dimensional space. The 2D positions are iteratively refined in order to minimize the divergence between the high-dimensional and two-dimensional distributions.

More specifically, a high-dimensional pairwise distance measure can be defined between all points. The similarity of data points $\mathbf{x_i}$ and $\mathbf{x_j}$ is expressed as the conditional probability, $p_{j|i}$, that $\mathbf{x_i}$ would pick $\mathbf{x_j}$ as its neighbor under the assumption that neighbors are picked in proportion to their probability density under a Gaussian centered at $\mathbf{x_i}$ (*31*):

$$p_{j|i} = \frac{\exp\left(-\left\|\boldsymbol{x_i} - \boldsymbol{x_j}\right\|^2 / 2\sigma_i^2\right)}{\sum_{k \neq i} \exp(-\|\boldsymbol{x_i} - \boldsymbol{x_k}\|^2 / 2\sigma_i^2)}, \tag{9}$$

and as the symmetrized conditional probabilities

$$p_{ij} = \frac{p_{j|i} + p_{i|j}}{2n}, \tag{10}$$

where n is the number of data points. The variance of the Gaussian, σ_i^2, is determined by a binary search in order to obtain a user-specified value for the *Perplexity*, which is defined as

$$Perplexity(P_i) = 2^{H(P_i)}, \tag{11}$$

where $H(P_i)$ is Shannon's entropy

$$H(P_i) = -\sum_j p_{j|i} \log_2 p_{j|i} \tag{12}$$

and P_i is the conditional probability distribution over all other data points given $\mathbf{x_i}$. The perplexity is, loosely speaking, controlling the number of close neighbors of each point and can have a complex non-linear influence of the resulting distribution of points.

The conditional probability $q_{j|i}$ of two points $\mathbf{y_i}$ and $\mathbf{y_j}$ in the two-dimensional space is modelled by a t-distribution:

$$q_{ij} = \frac{\left(1 + \left\|\boldsymbol{y_i} - \boldsymbol{y_j}\right\|^2\right)^{-1}}{\sum_{k \neq l} (1 + \|\boldsymbol{y_k} - \boldsymbol{y_l}\|^2)^{-1}} \tag{13}$$

The algorithm first randomly assigns a position to each data point in two-dimensional space and then iteratively refines the position of data points such as to minimize the Kullback-Leibler (KL) divergence, a natural measure for the mismatch between the joint probability distributions in the high-dimensional space, P, and in the low-dimensional space, Q. Thus, the cost function at every iteration is the KL divergence between P and Q,

$$KL(P||Q) = \sum_i \sum_j p_{ij} \log\left(\frac{p_{ij}}{q_{ij}}\right), \tag{14}$$

which is minimized using a gradient descent method. In other words, the two-dimensional position y_i is modified such as to minimize the KL divergence between P and Q. This minimization scheme depends critically on the conditional probabilities p_{ij} and q_{ij} and therefore on the distance $\|\cdot\|$ between points and the perplexity. We tested the influence of different distance metrics and perplexity values on our data set to exclude artifacts arising through an improper choice of parameters. The following distance metrics were tested:

1) Euclidian distance

$$\|\boldsymbol{x_i} - \boldsymbol{x_j}\| = \sqrt{(\boldsymbol{x_i} - \boldsymbol{x_j})^T (\boldsymbol{x_i} - \boldsymbol{x_j})} \tag{15}$$

2) Mahalanobis distance

$$\|\boldsymbol{x_i} - \boldsymbol{x_j}\| = \sqrt{(\boldsymbol{x_i} - \boldsymbol{x_j})^T S^{-1} (\boldsymbol{x_i} - \boldsymbol{x_j})} \tag{16}$$

where S is the covariance matrix. The Mahalanobis distance reduces to the Euclidian distance if S is the identity matrix.

3) Correlation distance

$$\|\boldsymbol{x_i} - \boldsymbol{x_j}\| = 1 - \frac{(\boldsymbol{x_i} - \overline{\boldsymbol{x_i}})^T (\boldsymbol{x_j} - \overline{\boldsymbol{x_j}})}{\sqrt{(\boldsymbol{x_i} - \overline{\boldsymbol{x_i}})^T (\boldsymbol{x_i} - \overline{\boldsymbol{x_i}})} \sqrt{(\boldsymbol{x_j} - \overline{\boldsymbol{x_j}})^T (\boldsymbol{x_j} - \overline{\boldsymbol{x_j}})}} \tag{17}$$

where $\overline{\boldsymbol{x}}$ denotes the average value of $\boldsymbol{x_i}$.

Perplexity values were varied from 30 to 200. Note that t-SNE is a probabilistic approach since points are initially distributed randomly in two dimensions. Therefore, multiple runs on the same data set might result in varying results.

Exemplary t-SNE maps are shown in Supplementary Figure 10A for the tested perplexity values and distance metrics. Maps are colored corresponding to Figure 6D. The embedding of points in two dimensions varies greatly among the scenarios. However, the probability of two points being nearest neighbors is largely conserved and thus ranking of input parameters yield similar results across the employed scenarios (Supplementary Figure 10B). Rankings are especially robust when the distance metric is the Euclidian distance or the Mahalanobis distance. When the correlation distance is employed, the rankings slightly change. Especially, the area of blobs seems to be more prominent than the flow magnitude, in contrast to rankings when one of the other distance metrics is used. However, rankings change only to a small extent among the different distance metrics and perplexity values and the presented results are therefore free of artifacts of t-SNE or algorithm-dependent parameters.

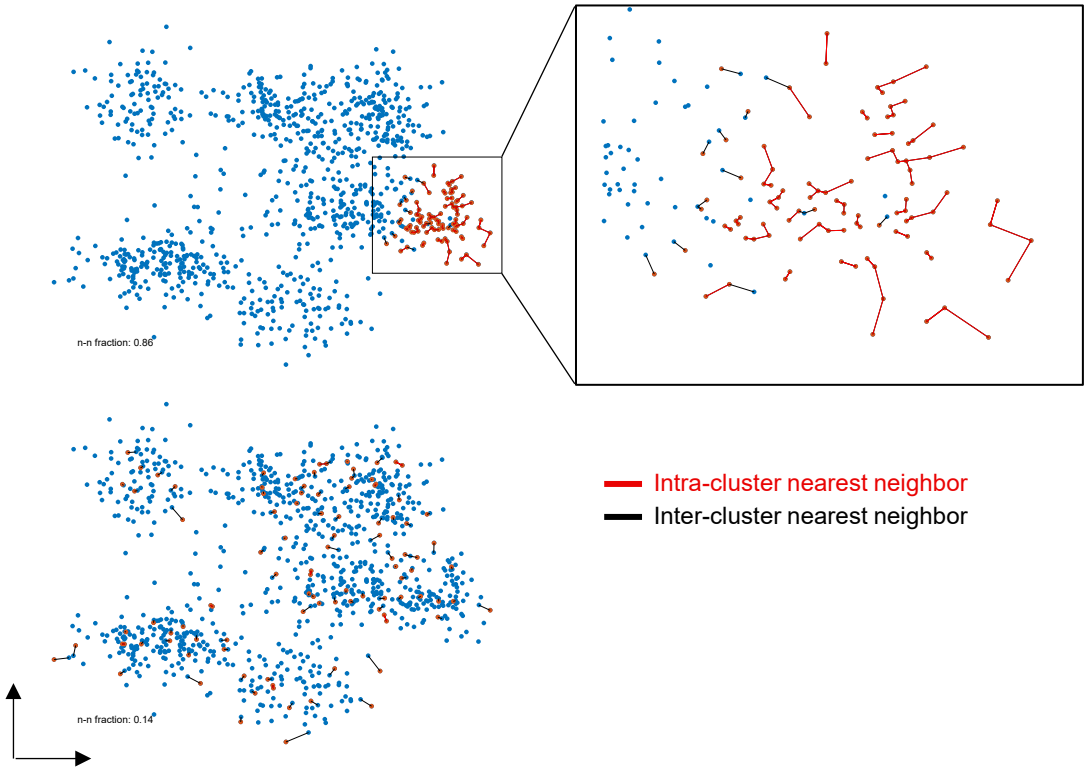

Supplementary Figure 9: Clustering illustration of points within a subset based on nearest-neighbors in t-SNE maps. Dimension reduction using t-SNE results in point clouds in which nearest neighbors in high-dimensional space are conserved and mapped as nearest neighbors in two dimensions. Points at which a number of interest exhibits unusually high/low values are identified (red points). Mapping of two points as nearest neighbors in reduced t-SNE space can be because nearest neighbors belong to the same subset of high/low values of a variable of interest. To quantify this empirical characteristic, the number of nearest neighbors within the same subset in t-SNE space is counted relative to the total number of nearest neighbors of all points within the subset. **A)** A subset mostly contains its own nearest neighbors (86% of nearest neighbors of all points in the subset are contained within the subset). The magnification shows nearest neighbor connections within the subset (red lines) and between points in the subset and points not contained in the subset (black lines). **B)** Points within the subset are distributed over the whole t-SNE space and thus do not form a grouped region. The fraction of nearest neighbor links within the subset is small (14%) compared to the clustered case.

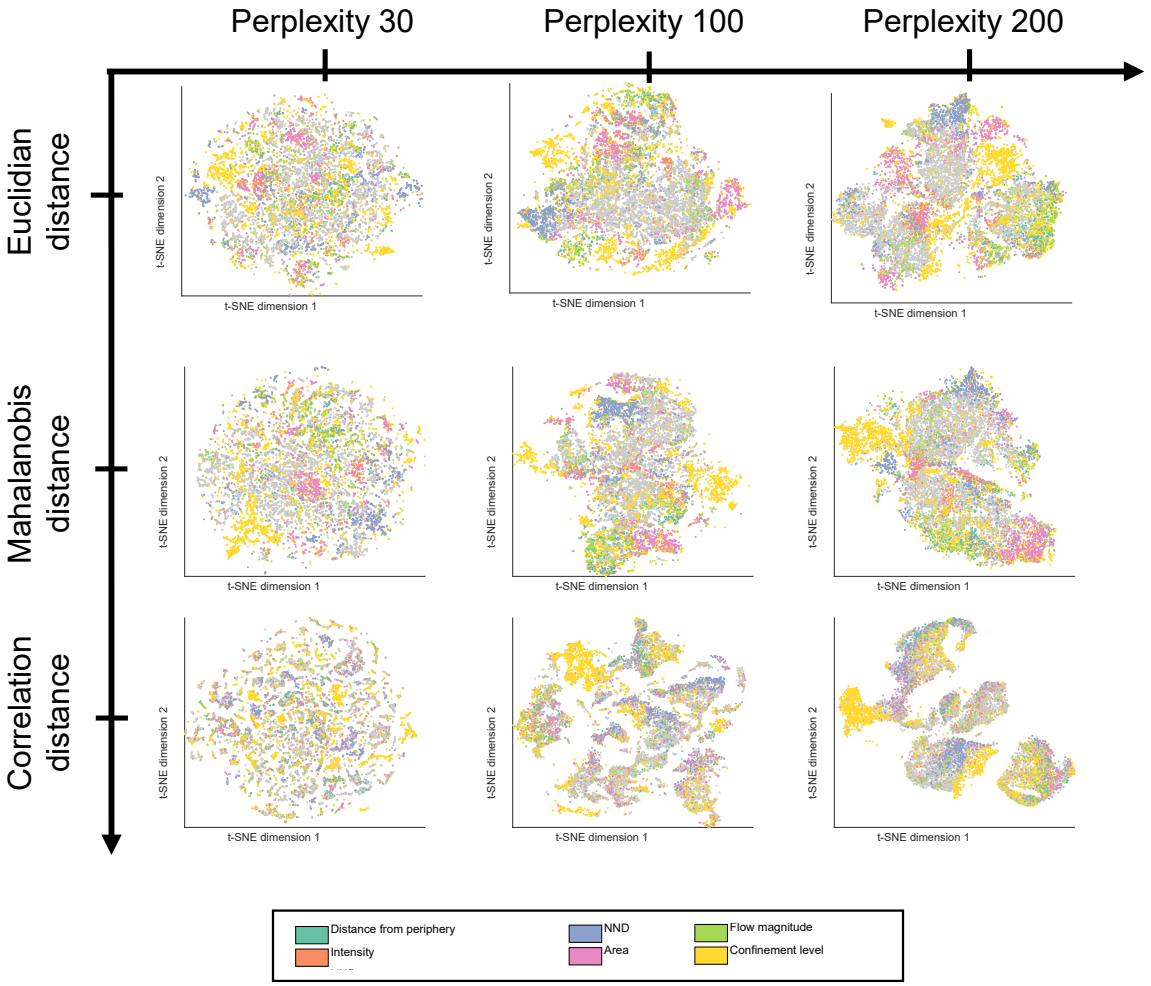
Perplexity 30
Perplexity 100
Perplexity 200
Euclidian distance
Mahalanobis distance
Correlation distance
t-SNE dimension 1
t-SNE dimension 2
Distance from periphery
Intensity
NND
Area
Flow magnitude
Confinement level

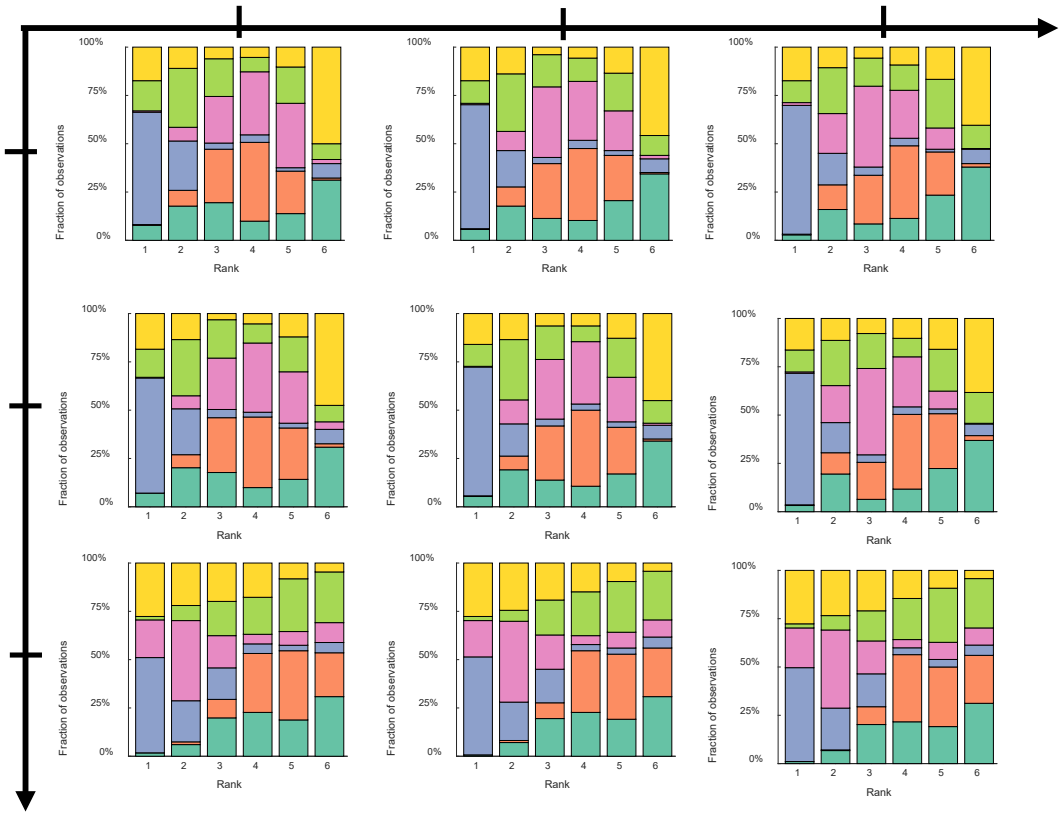
Fraction of observations
Rank
0%
25%
50%
75%
100%
1
2
3
4
5
6

Supplementary Figure 10: t-SNE for different distance metrics and perplexity values. We tested the influence of different distance measures between the high-dimensional data points as well as variations in the perplexity from 30 to 200 and found that our data are robust to changes in these parameters within the explored range. **A)** Exemplary t-SNE maps and **B)** feature ranking considering various distance metrics and values for the perplexity parameter applied to our data.